Electrochimica Acta 452 (2023) 142263

Contents lists available at ScienceDirect

Electrochimica Acta

journal homepage: www.journals.elsevier.com/electrochimica-acta

Reciprocal irreversibility compensation of $LiNi_{0.2}Co_{0.2}Al_{0.1}Mn_{0.45}O_2$ cathode and silicon oxide anode in new Li-ion battery

Luca Minnetti [a], Vittorio Marangon [b,c], Paolo Andreotti [c], Antunes Staffolani [a], Francesco Nobili [a,*], Jusef Hassoun [b,c,d,*]

[a] School of Sciences and Technologies – Chemistry Division, University of Camerino, Via Madonna delle Carceri ChIP, Camerino 62032, Italy
[b] Graphene Labs, Istituto Italiano di Tecnologia, via Morego 30, Genoa 16163, Italy
[c] Department of Chemical, Pharmaceutical and Agricultural Sciences, University of Ferrara, Via Fossato di Mortara 17, Ferrara 44121, Italy
[d] National Interuniversity Consortium of Materials Science and Technology (INSTM) University of Ferrara Research Unit, University of Ferrara, Via Fossato di Mortara, 17, Ferrara 44121, Italy

ARTICLE INFO

Keywords:
$LiNi_{0.2}Co_{0.2}Al_{0.1}Mn_{0.45}O_2$ cathode
Silicon oxide anode
Synthesis
Li-ion battery
Cell balance

ABSTRACT

A layered $LiNi_{0.2}Co_{0.2}Al_{0.1}Mn_{0.45}O_2$ cathode is herein synthetized and investigated. Scanning electron microscopy (SEM) shows the layered morphology of the composite powder, while energy dispersive X-ray spectroscopy (EDS) and Inductively Coupled Plasma-Mass Spectrometry (ICP-MS) confirm the achieved stoichiometry. X-ray diffraction (XRD) well identifies the layered structure unit cell, and Raman spectroscopy displays the corresponding M-O bonds motions. The cycling voltammetry (CV) of $LiNi_{0.2}Co_{0.2}Al_{0.1}Mn_{0.45}O_2$ in lithium half-cell reveals an electrochemical process characterized by a remarkable irreversible oxidation taking place at 4.6 V *vs.* Li^+/Li during the first scan, and subsequent reversible Li (de)intercalation centered at 3.8 V *vs.* Li^+/Li with interphase resistance limited to 16 Ω upon activation as indicated by electrochemical impedance spectroscopy (EIS). The relevant irreversibility during first charge is also detected by galvanostatic cycling in a lithium half-cell subsequently operating at an average voltage of 3.8 V with a stable trend, and a maximum specific capacity of 130 mAh g^{-1}. The initial irreversible capacity of the layered cathode is advantageously exploited for compensating the pristine inefficiency of the Li-alloying composite anode in a proof-of-concept Li-ion battery achieved by combining the $LiNi_{0.2}Co_{0.2}Al_{0.1}Mn_{0.45}O_2$ with a silicon oxide composite (SiO_x-C) without any preliminary pretreatment of the electrodes. The full-cell displays a cycling behavior strongly influenced by the anode/cathode ratio, and the corresponding EIS performed both on the single electrodes and on the Li-ion cell by using an additional lithium reference suggests a controlling role of the anode interphase and possible enhancements through a slight excess of cathode material.

1. Introduction

Lithium-ion batteries (LIBs) are presently the systems of choice for powering the portable electronics, the most promising candidate for driving the electric vehicles (EVs) to limit greenhouse gasses emission [1,2], and a possible energy storage system from renewable sources to mitigate the high inflation related to pandemic and geo-political shocks [3]. The massive diffusion of this ground-breaking technology actually triggered a rapid development of EVs, and posed concerns on the present systems due to challenging market requirements such as the long driving autonomy, high safety level, and an adequate price [4,5]. Therefore, a remarkable deal of efforts is nowadays devoted towards LIBs optimization strategies including anode, cathode and electrolyte sides [4–7]. Accordingly, the typical $LiCoO_2$ layered cathode has been almost fully replaced by multi-metal oxides of the same structure such as Li($Ni_xCo_yMn_{1-x-y}$)O_2, in which the expensive and toxic cobalt is partially or totally substituted with other transition metals, thus achieving further bonuses including adequate operating voltage, specific capacity, and thermal stability of the de-lithiated phase [8–11]. Despite the remarkable performance of widely employed electrodes such as $LiNi_{1/3}Co_{1/3}Mn_{1/3}O_2$ (NMC333) and $LiNi_{0.8}Co_{0.1}Mn_{0.1}O_2$ (NMC811) [12,13], the layered oxides still suffer from capacity decay upon prolonged cycling and possible safety issues due to phase changes involving material delamination and oxygen loss at the charged (de-lithiated) state

* Corresponding authors.
E-mail addresses: francesco.nobili@unicam.it (F. Nobili), jusef.hassoun@unife.it (J. Hassoun).

https://doi.org/10.1016/j.electacta.2023.142263
Received 23 January 2023; Received in revised form 9 March 2023; Accepted 15 March 2023
Available online 20 March 2023

[14,15]. This side reaction during the first cycle has also been reported as one of the main issues of voltage hysteresis during subsequent cycles, in particular in Li-rich layered oxides, which causes instability of the structure during redox processes [16]. Moreover, layered oxide cathodes with different alkali ions (*e.g.* Na) suffer from the same issue, reflected in a reorganization from P2 to O3-type structure that inhibits the cell performance [17,18]. Various strategies have been adopted to enhance the NMC stability, such as metal doping [19–21], acid treatment [22], and partial substitution of cobalt with aluminum which may represent a viable approach due to the stabilizing effect of Al already observed for the α-$NaFeO_2$-type layered structure [23–25]. Regarding the anode side, the interest of the scientific community principally focused on Li-alloy composites including Si [26,27], Sn [28–30], Sb [31] SnO_2 [32,33], SiO_x [34–36], and Li-conversion oxides such as Fe_2O_3 [37], and NiO [38] due to the higher specific capacity delivered with respect to the conventional graphite [39]. On the other hand, the combination between substituted layered cathodes and Li-alloy conversion anodes is an attractive strategy to enhance the energy content and environmental compatibility of Li-ion batteries [40,41], despite the still open issues ascribed to these families of electrodes. Indeed, layered cathode materials may be affected by irreversible charge (de-lithiation) process during first cycle ascribed to a structural reorganization of the electrode by oxidation [42], while the alloy anodes suffer by a relevant irreversibility during first discharge (lithiation) due to matrix modification and solid electrolyte interphase (SEI) layer reductive formation concomitantly with the Li-alloying process [33]. This behavior posed intrinsic issues on the direct combination of the above electrodes in an efficient Li-ion cell, without *ad-hoc* designed *pre-activation* procedures including preliminary electrochemical or chemical lithiation, in particular of the anode, before their use [42,43]. In fact, possible irreversibility on the cathode or anode may lead to the loss of the cell balance in terms of negative to positive (N/P) ratio and finally affect both the delivered capacity and the cycling stability of the Li-ion battery [44]. In this scenario, we propose and thoroughly characterize a multi-metal substituted $LiNi_{0.2}Co_{0.2}Al_{0.1}Mn_{0.45}O_2$ layered cathode for direct application in full Li-ion battery using a pristine carbon-coated SiO_x anode (SiO_x-C) without any further treatment of the electrodes before use in cell. Therefore, the remarkable irreversible capacity observed in the $LiNi_{0.2}Co_{0.2}Al_{0.1}Mn_{0.45}O_2$ cathode during the first charge due to its specific composition is advantageously exploited to balance the intrinsic SiO_x-C anode irreversibility, thus allowing a preliminary control of the full-cell behavior by adequately selecting the N/P ratio. This novel combination, and the alternative approach adopted to achieve Li-ion full-cells with promising performances, may be of actual interest for allowing the exploitation of alternative materials with physical-chemical characteristics different than those of diffused electrodes in the commercially available LIBs.

2. Experimental section

2.1. Synthesis of $LiNi_{0.2}Co_{0.2}Al_{0.1}Mn_{0.45}O_2$ cathode and SiO_x-C anode

3 g of $LiNi_{0.2}Co_{0.2}Al_{0.1}Mn_{0.45}O_2$ material, subsequently indicated with the acronym LNCAM, was synthetized through a co-precipitation method, according to previous works principally focused on Na-layered electrodes [45,46]. 1.3246 g of aluminum nitrate nonahydrate ($Al(NO_3)_3{\cdot}9H_2O$, Sigma-Aldrich, ≥98.0%), 2.0553 g of cobalt-(II)-nitrate hexahydrate ($Co(NO_3)_2{\cdot}6H_2O$, Sigma-Aldrich, ≥99.0%), 2.0536 g of nickel-(II)-nitrate hexahydrate ($Ni(NO_3)_2{\cdot}6H_2O$, Sigma-Aldrich, ≥98.5%), and 3.9885 g of manganese-(II)-nitrate tetrahydrate ($Mn(NO_3)_2{\cdot}4H_2O$, Sigma-Aldrich, ≥97.0%) were dissolved in 100 mL of deionized water to form a solution with a Al/Co/Ni/Mn molar ratio of 0.1:0.2:0.2:0.45. Then, 4.2370 g of NaOH pellets (≥98%, Sigma-Aldrich) was dissolved in 212 mL of deionized water to obtain a 0.5 M NaOH aqueous solution which was added dropwise to the nitrate solution. The nitrate-NaOH solution using a 50 mol% excess of NaOH with respect to nitrate was stirred for 12 h to precipitate a hydroxide precursor that was filtered, washed with deionized water and ethanol until a pH of 7, dried overnight at 70 °C in oven, and calcinated for 12 h at 120 °C (heating rate of 2 °C min^{-1}) in a dry air flow. Afterward, the hydroxide precursor was ground in an agate mortar with lithium hydroxide hydrate ($LiOH{\cdot}H_2O$, ≥98%, Sigma-Aldrich) in the 1:1 molar ratio and the resulting mixture was pelletized and calcinated under a dry air flow at 500 °C (heating rate of 5 °C min^{-1}) for 5 h to obtain the material indicated with the acronym LNCAM500. The LNCAM500 precursor was ground in an agate mortar, pelletized and calcinated under a dry air flow at 1000 °C (heating rate of 5 °C min^{-1}) for 6 h to obtain the material indicated with the acronym LNCAM1000_6h, which was ground, pelletized and calcinated under a dry air flow at 1000 °C (heating rate of 5 °C min^{-1}) for 12 h to obtain the final cathode indicated with the acronym LNCAM1000_12h. All the thermal steps of the synthesis procedure were performed in a GHA 12/3000 (Carbolite) tubular furnace. The SiO_x-based anode material (indicated as SiO_x-C) was synthetized as reported in a previous paper [27]. 18 g of resorcinol was added to 58.5 g of formaldehyde at room temperature and 21 g of tetraethyl orthosilicate (TEOS) was dissolved in the homogeneous mixture. The achieved solution was heated at 70 °C and 2 mL of HCl (1 M) was added dropwise to catalyze the formation of a pink gel, which was aged for 24 h at room temperature, cut into pieces, washed with ethanol to remove residual HCl, and annealed at 1000 °C for 10 h under Ar-H_2 (5%) flow. The obtained SiO_x-C powder was finally ground in a mortar.

2.2. Materials characterization

Scanning electron microscopy (SEM) images of the LNCAM_1000_12h sample were acquired by a Zeiss EVO 40 microscope with a LaB_6 thermionic source. Energy dispersive X-ray spectroscopy (EDS) was performed on the SEM images via a X-ACT Cambridge Instruments analyzer to record elemental maps and estimate the LNCAM1000_12h stoichiometry. The elemental composition of the sample was also determined via Inductively Coupled Plasma-Mass Spectrometry (ICP-MS) technique. HNO_3 (70%, ≥99.999% trace metal basis, Sigma-Aldrich) and HCl (37%, for analysis-ISO, Carlo Erba reagents) were used without any further purifications. Ultrapure H_2O (18 MΩ cm) was used for the dilution of the sample. 100 mg of LNCAM1000_12h was digested in 5 mL of aqua regia (HNO_3:HCl 1:3 molar ratio) at 120 °C for 1 h by using a Parr 4744 acid digestion vessel (Parr Instrument Company). After cooldown, the solution was diluted to the proper concentration prior the ICP-MS analysis. An ICP-MS Agilent 7500 (Agilent Technologies inc.) equipped with a 3 MHz quadrupole was used for the metal determination. X-ray diffraction (XRD) patterns of the LNCAM500, LNCAM1000_6h and LNCAM1000_12h materials were collected by performing scans in the 2θ range from 10° to 90° at a rate of 10 s $step^{-1}$ with step size of 0.02° through a Bruker D8 Advance instrument using a Cu-Kα source and a graphite monochromator on the diffracted beam. Rietveld refinement of the LNCAM1000_12h pattern was carried out through the MAUD software [47] by using the reference parameters of the $LiNi_{0.4}Co_{0.15}Al_{0.05}Mn_{0.4}O_2$ layered oxide (*R*-3 m space group, N. 166, ICSD #166,715) [25]. The refinement was carried out by fixing atom occupancies to the values estimated by EDS and the isotropic atomic displacement parameters were set to the same value for Al, Mn, Co, and Ni upon the refinement. Raman spectroscopy was performed on the LNCAM1000_12h powder through a Czerny-Turner spectrometer (iHR320 Horiba Scientific) equipped with a diffraction grating of 1800 grooves mm^{-1} and a laser source with λ = 532 nm. Thermogravimetric measurement on SiO_x-C powder was carried out under air flow employing a heating rate of 5 °C min^{-1} in the 25 – 800 °C temperature range through a Mettler-Toledo TGA 2 instrument.

2.3. Electrode preparation

The electrode slurries were prepared by dispersing the active

material (either LNCAM1000_12h or SiO_x-C), polyvinylidene fluoride (PVDF 6020 Solef®) binding polymer and carbon black (Super P carbon, Timcal) mixed by the 8:1:1 wt ratio in *N*-methyl-2-pyrrolidone (NMP, Sigma-Aldrich) and were stirred at room temperature until homogenization (about 1 h). The slurries were cast by a doctor blade tool on either aluminum carbon-coated foils (thickness ~ 20 μm, MTI Corporation) for LNCAM1000_12h or scratched copper foils (thickness ~ 30 μm, MTI Corporation) for SiO_x-C. The electrode tapes were dried for 3 h on a hot plate at 70 °C, cut into disks with diameter of either 10 mm or 14 mm, and dried for 3 h at 110 °C under vacuum to remove possible residual traces of water and NMP solvent. Prior to vacuum drying, LNCAM1000_12h electrodes were pressed with a hydraulic press (Silfradent) for 30 s at 115 bar. The final active material loading ranged from 4 to 4.5 mg cm^{-2} for LNCAM1000_12h and from 1.2 to 1.8 mg cm^{-2} for SiO_x-C, as normalized to the electrode geometric area (either 0.785 or 1.54 cm^2 for electrodes with a diameter of 10 mm or 14 mm, respectively). Carbon/PVDF electrodes coated on Al foil (thickness ~ 15 μm, MTI Corporation) indicated as SPC-Al were prepared by the doctor blade casting procedure described above using Super P carbon and PVDF binder in the 80:20 wt ratio, cut into 10 mm disks, and dried at 110 °C for 3 h under vacuum.

2.4. Cell assembly

Two-electrode Swagelok T-type lithium half-cells were assembled by stacking a 10 mm-diameter LNCAM1000_12h cathode, a 10 mm-diameter lithium metal anode (MTI Corporation) and a 10 mm-diameter glass fiber Whatman® GF/B disk as the separator. The EC:DMC 1:1 v/v 1 M $LiPF_6$ solution (Sigma-Aldrich) was used as electrolyte and consisted of ethylene carbonate (EC) and dimethyl carbonate (DMC) solvents mixed in the 1:1 vol ratio dissolving lithium hexafluorophosphate ($LiPF_6$) in concentration of 1 mol $dm^{-3}_{solution}$ (1 M). Three-electrode Swagelok T-type lithium half-cells were prepared with the same configuration by using an additional 10 mm-diameter lithium metal disk as the reference electrode at the top side of the T-cell. An additional three-electrode Swagelok T-type lithium cell was prepared using a 10 mm-diameter SPC-Al electrode as cathode, a 10 mm-diameter lithium metal anode, a 10 mm-diameter Celgard 2400 as the separator, and an additional 10 mm lithium metal disk as the reference electrode. CR2032 coin-type lithium half-cells (MTI Corporation) were assembled by using the LNCAM1000_12h cathode and a lithium metal anode both with diameter of 14 mm separated by a 16 mm-diameter glass fiber Whatman® GF/B disk. Three-electrode Swagelok-type full-cells were assembled by stacking a LNCAM1000_12 h cathode, a SiO_x-C anode, one glass fiber Whatman® GF/B separator and an additional lithium metal disk as the reference electrode placed at the top side of the T-cell. An additional CR2032 coin-type full cell was assembled by using a 14 mm-diameter LNCAM1000_12h cathode, a 14 mm-diameter SiO_x-C anode, and one 16 mm-diameter glass fiber Whatman® GF/B separator. The SiO_x-C|LNCAM1000_12h full-cells were prepared by using negative to positive (N/P) capacity ratios of 0.98 or 0.84 (for Three-electrode cells), and 0.91 (for Coin-type cell), as determined by taking into account mass loadings and specific capacities of the two electrodes at the first charge of a full-cell, that is, 300 mAh g^{-1} for cathode first de-lithiation and 810 mAh g^{-1} for anode first lithiation. Hence, electrode loadings of 1.53 mg_{anode} cm^{-2} and 4.21 $mg_{cathode}$ cm^{-2} was used for $N/P = 0.98$, 1.26 mg_{anode} cm^{-2} and 4.05 $mg_{cathode}$ cm^{-2} for $N/P = 0.84$, and 1.75 mg_{anode} cm^{-2} and 5.19 $mg_{cathode}$ cm^{-2} for $N/P = 0.91$. All cells were assembled and sealed inside an Ar-filled glovebox (MBraun, O_2 and H_2O content lower than 1 ppm).

2.5. Electrochemical tests and ex-situ measurements

A preliminary Linear sweep voltammetry (LSV) was performed to evaluate the EC:DMC 1:1 v/v 1 M $LiPF_6$ electrolyte anodic stability in lithium battery using a three-electrode T-type cell with SPC-Al electrode at a scan rate of 0.1 mV s^{-1} from the OCV condition of the cell to 6 V *vs.* Li^+/Li. Cyclic voltammetry (CV) was performed using a three-electrode Li|LNCAM1000_12h half-cell at a scan rate of 0.1 mV s^{-1} in the 2.5 – 4.9 V *vs.* Li^+/Li potential range, while electrochemical impedance spectroscopy (EIS) was collected at the open circuit voltage (OCV) condition of the cell as well as after 1, 5, and 10 CV cycles by applying an alternate voltage signal of 10 mV in the 500 kHz – 100 mHz frequency range. Galvanostatic cycling measurements were performed on CR2032-type Li|LNCAM1000_12h half-cells at the constant current rate of C/20 (1C = 298 mA g^{-1}) in the voltage ranges of 2.5 – 4.4 V, 2.5 – 4.8 V, and 2.5 – 4.9 V by adopting the constant-current constant-voltage (CCCV) mode, that is, by setting an additional constant voltage step during charge at either 4.4 V, 4.8 V, or 4.9 V, respectively, until a current value of ¼ of the initial C-rate was reached. *Ex-situ* XRD measurements were performed on LNCAM1000_12h electrodes retrieved from two-electrode Swagelok-type lithium half-cells upon either 1 or 2 charge/discharge cycles at C/20 between 2.5 and 4.9 V by adopting the CCCV mode at 4.9 V during charge. XRD scans of the cycled electrodes and of a pristine one were collected by a Bruker D8 Advance instrument using a Cu-Kα source and a graphite monochromator on the diffracted beam in the 10° – 60° 2θ range at a rate of 10 s $step^{-1}$ and a step size of 0.02°. Prior to XRD investigation, the cycled electrodes were washed with DMC solvent and dried at 25 °C under vacuum for 30 min. A rate capability test was performed on a CR2032-type Li| LNCAM1000_12h half-cell by increasing the current rate from C/10 to C/8, C/5, C/3 and 1C every 5 cycles and lowering back to C/10 after 25 cycles. The test was performed between 2.5 and 4.8 V by adopting the CCCV mode at 4.8 V during charge. CR2032-type Li|LNCAM1000_12h half-cells were galvanostatically cycled at the constant current rate of either C/10 or C/5 between 2.5 and 4.8 V by using the CCCV mode at 4.8 V during charge. Full SiO_x-C|LNCAM1000_12h cells were galvanostatically cycled at the constant rate of C/10 (1C = 298 mA $g^{-1}_{cathode}$) in the 1.5 – 4.8 V voltage range by adopting the CCCV mode at 4.8 V during charge. EIS measurements were performed on the three-electrodes SiO_x-C|LNCAM1000_12h cells at the OCV condition and after 1 and 10 galvanostatic cycles by using an alternate voltage signal of 30 mV in the 500 kHz – 100 mHz frequency range. All the Nyquist plots recorded by EIS were analyzed through the non-linear least squares (NLLS) fitting method by using the Boukamp software and only fits with χ^2 values of the order of 10^{-4} or lower were accepted [48,49]. CV and EIS were carried out by a VersaSTAT MC Princeton Applied Research (PAR, AMETEK) instrument, while the charge/discharge cycling tests were performed by a MACCOR series 4000 battery test system. All the data were recorded at the room temperature (25 °C).

3. Results and discussion

The morphology of the LNCAM1000_12h cathode material is investigated by SEM-EDS analysis, as reported in Fig. 1. The SEM images of the powder show flakes with size ranging from 3 to 25 μm characterized by a layered morphology (Fig. 1a) stacked into submicrometric primary particles with nanometric thickness (Fig. 1b). The corresponding EDS elemental maps acquired on SEM imaging (Fig. 1c) of O (Fig. 1d), Al (Fig. 1e), Mn (Fig. 1f), Co (Fig. 1g), and Ni (Fig. 1h) display a homogeneous distribution of the elements, without impurities as confirmed by the EDS spectrum in Figure S1 in the Supplementary Material. However, the elemental mapping in Fig. 1g evidences the presence of more intense Co X-ray signals inferred from few regions suggesting a slight Co segregation and crystalline agglomeration in the sample already observed for similar materials [50]. The EDS also allows the determination of a $LiNi_{0.18}Co_{0.20}Al_{0.09}Mn_{0.43}O_2$ stoichiometry which well approaches the one designed during synthesis, *i.e.*, $LiNi_{0.2}Co_{0.2}Al_{0.1}Mn_{0.45}O_2$ (see Table 1), thus suggesting the successful incorporation of the transition metals into the material [46]. A similar result, reported in Table 1, is obtained by ICP-MS measurement that likely confirms the material stoichiometry discussed above. XRD

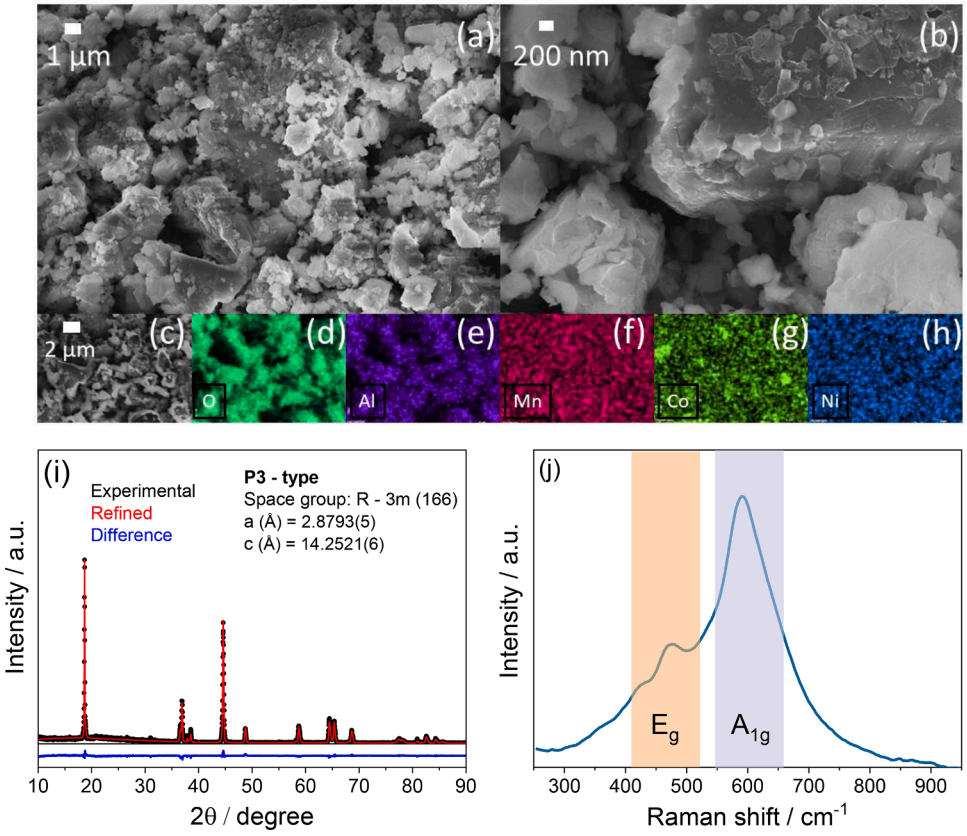

Fig. 1. Characterization of the LNCAM1000_12h material. **(a, b)** SEM images at different magnifications; **(c-h)** SEM-EDS analyses with elemental maps of **(d)** O, **(e)** Al, **(f)** Mn, **(g)** Co and **(h)** Ni; **(i)** XRD and corresponding Rietveld refinement (R-3*m* space group, table n. 166) showing experimental pattern (black dots), calculated pattern (red line) and difference profile (blue line); **(j)** Raman spectrum recorded in the 250 – 950 cm^{-1} range. Highlighted regions report transitions identification. See the Experimental section for acronyms.

Table 1
Comparison of EDS and ICP-MS outcomes in terms of average atomic% (EDS), stoichiometric coefficient (EDS), concentration (ICP-MS), and stoichiometric coefficient (ICP-MS) for Li, Ni, Co, Al, Mn, and O in LNCAM1000_12h. See corresponding EDS spectrum in Figure S1 (Supplementary Material) and Experimental section for acronyms.

Element	EDS Average Atomic%	EDS Stoichiometric coefficient	ICP-MS Concentration (ppb)	ICP-MS Stoichiometric coefficient
Li	/	/	64.16	1.00
Ni	6.11	0.18	95.15	0.18
Co	6.76	0.2	99.33	0.18
Al	2.96	0.09	33.92	0.14
Mn	14.93	0.43	211.4	0.42
O	69.24	2.00	/	/

measurements are performed on LNCAM1000_12h, as well as on the LNCAM500 and LNCAM1000_6h precursors to investigate the samples' structure, as reported in Fig. 1i and Figure S2 in the Supplementary Material, respectively. The comparison between the XRD patterns of the LNCAM materials during the synthesis (Figure S2) displays the growth of the crystalline phase by the subsequent steps and the formation of the P3-type layered structure in the final LNCAM1000_12h sample. Moreover, the progressive definition of the (006)/(012) peaks couple at 37.82°/38.32° and the (018)/(110) one at 64.48°/65.44° indicates the consolidation of the hexagonal ordering of the LNCAM layered structure, which is confirmed by a R value of about 0.51 where R is defined as the $(I_{006}/I_{102})/I_{101}$ intensities ratio [51]. Additional structural insights are provided by the Rietveld refinement of the LNCAM1000_12h XRD pattern in Fig. 1i carried out by constraining the atom occupancy according to the EDS results (Figure S1 in the Supplementary Material). The refined diffractogram (red dots in Fig. 1i) confirms a trigonal cell unit (hexagonal *R*-3*m* space group, table n. 166) without significant content of impurities, as also suggested by the difference profile [25]. The lattice parameters determined by refinement, that is, *a, c, c/a* and cell volume, are reported in Table 2 and compared with those of the $LiNi_{0.4}Co_{0.15}Al_{0.05}Mn_{0.4}O_2$ (ICSD #166715) [51,52]. The LNCAM1000_12h shows slightly different *a* and *c* values leading to a higher cell volume of 102.32 $Å^3$ compared to the 101.99 $Å^3$ of the reference, likely due to the higher content of Mn [53]. Furthermore, Table 2 reveals a *c/a* ratio of about 4.95, which indicates a well ordered structure of the sample [54], and a 003/104 peaks intensity ratio (I_{003}/I_{104}, see Figure S2 in the Supplementary Material for peaks indexing) exceeding 1.5, thus suggesting a low degree of cation mixing, in particular for the Ni^{2+} occupancy in the Li^+ sites, and likely an enhanced Li^+ ions mobility within the cathode [54]. The accuracy of the Rietveld refinement is suggested by a goodness-of-fit parameter (GOF) and weighted-profile R factor (R_{wp}%) values lower than 2 and 20, respectively (Table 2) [55]. The Raman spectroscopy performed on LNCAM1000_12h in Fig. 1j further confirms the layered structure by exhibiting two main peaks around 476 cm^{-1}, related to the symmetric stretching vibration of the M–O bond (E_g symmetry), and at 590 cm^{-1}, assigned to the O–M–O bending vibration (A_{1g} symmetry) [56,57]. In summary, LNCAM1000_12h displays defined layered morphology and structure with uniform distribution of the elements that are crucial parameters to enable the formation of a suitable electrode/electrolyte interphase in lithium cell and satisfactory cycling behavior [58], since irregular layer stacking or excessive aggregation may hinder the Li^+ ions diffusion in the material framework [59].

Prior to testing the cell applicability of the LNCAM1000_12h electrode, the anodic electrochemical stability of the electrolyte (*i.e.*, EC: DMC 1:1 v/v 1 M $LiPF_6$) is checked in Figure S3 (Supplementary Material). The LSV shows a small increase of the current around 5 V *vs.* Li^+/Li and full oxidative decomposition at 5.2 V *vs.* Li^+/Li, thus in full agreement with various literature reports [60–62]. The electrochemical process of the LNCAM1000_12h cathode is subsequently investigated in

Table 2
Results of Rietveld refinement in terms of lattice parameters, unit cell volume, c/a parameters ratio, I_{003}/I_{104} intensities ratio, good-of-fit parameter (GOF), and weighted-profile R factor (R_{wp}%) of LNCAM1000_12h. Reference ICSD #166715 [25]. See corresponding diffractogram in Fig. 1 and Experimental section for acronyms.

Material	*a* (Å)	*c* (Å)	*c/a*	V (Å^3)	I_{003}/I_{104}	GOF (σ)	Rwp%
$LiNi_{0.4}Co_{0.15}Al_{0.05}Mn_{0.4}O_2$ (ICSD #166715)	2.872	14.273	4.969	101.99	1.848	/	/
LNCAM1000_12h	2.879(3)	14.252(1)	4.949(8)	102.32(5)	1.517(6)	1.50	17.18

lithium half-cell by combining CV and EIS measurements, as reported in Fig. 2. The CV response (Fig. 2a) shows during the first cycle two oxidation peaks centered at 4.0 V and 4.6 V *vs.* Li^+/Li and a single reduction wave merged at about 3.8 V *vs.* Li^+/Li. The above irreversible oxidation peak at 4.6 V *vs.* Li^+/Li is likely ascribed to partial oxygen loss due to structural rearrangement with possible phase modification of the cathode and concomitant partial electrolyte degradation [63], in particular the decrease of Co-O and Ni-O distances due to oxidation of the transition metals, and negligible changes in Mn-O distance which holds Mn^{4+} oxidation state [64]. Nevertheless, the charge and discharge signals at 4.0 and 3.8 V *vs.* Li^+/Li, respectively, are associated with the reversible (de)intercalation of the Li^+ ions into the layered structure [65]. The irreversible lithium extraction related to the additional oxidation peak at the first cycle centered at about 3.4 V *vs.* Li^+/Li may be ascribed to the presence of impurity traces in the electrolyte (*e.g.*, water or other solvents) as well as to possible side Ni^{2+}/Ni^{4+} oxidation process as suggested by literature reports [16]. However, the vanishing of the above peak during reduction and in the subsequent cycles suggests the formation of a suitable SEI layer at the electrodes surface [66]. During the subsequent voltammetry cycles, the electrochemical process reversibly evolves with a single oxidation peak at 3.9 V *vs.* Li^+/Li reflected into the corresponding reduction signal at 3.7 V *vs.* Li^+/Li. The slight shift of the oxidation process to lower potential upon the first cycle further suggests a favorable reorganization of the material structure, while the modest polarization certainly indicates the formation of a suitable SEI at the electrodes surface [66,67]. This aspect is additionally investigated by EIS measurements performed at the OCV condition of the cell as well as after 1, 5, and 10 CV scans (Fig. 2b).

The reported Nyquist plots are analyzed by NLLS method and the results are reported in Table 3 [48,49]. The graphs in Fig. 2b display a semicircle in the medium-high frequency region accounting for the Li^+ ion exchange through the electrode/electrolyte interphase, and a low-frequency almost vertical tilted line representing the cell geometrical capacity [68]. Therefore, the EIS can be represented by the $R_e(R_iQ_i)Q_g$ equivalent circuit, where R_e is the electrolyte resistance determined by the high-frequency intercept in the corresponding plot, the (R_iQ_i) elements reflect the main semicircle with a total resistance corresponding to the charge transfer at the electrode/electrolyte interphase and the SEI layer at the electrodes surface, while Q_g is a constant phase element related the cell capacitance [48,49]. After one cycle, the splitting of the SEI and charge transfer related features is clearly evidenced, thus allowing the fit of the two separate contributions, detailed in Table 3. Table 3 also reveals a trend by which the initial total interphase resistance at the OCV of 32 Ω decreases to about 5 Ω after 5 cycles, and stabilizes at 16 Ω at the end of the test. This behavior well supports the above mentioned formation of a suitable SEI and the favorable structural rearrangement of the cathode that may boost the reaction kinetics in lithium cell and enhance the corresponding performance [52].

Table 3
NLLS analyses of the Nyquist plots reported in Fig. 2 recorded by performing EIS on a Li|LNCAM1000_12h three-electrode cell. NLLS analyses were performed through a Boukamp software and only fits with a χ^2 value of the order of 10^{-4} or lower were considered suitable [48,49]. See Experimental section for acronyms.

Cell condition	Equivalent circuit	R_1 (Ω)	R_2 (Ω)	$R_i = R_1 + R_2$ (Ω)	χ^2
OCV	$R_e(R_1Q_1)Q_g$	32.3 ± 0.5	/	32.3 ± 0.5	6×10^{-4}
After 1 CV scan	$R_e(R_1Q_1)(R_2Q_2)Q_g$	7.6 ± 0.1	1.8 ± 0.1	9.4 ± 0.1	2×10^{-5}
After 5 CV scans	$R_e(R_1Q_1)Q_g$	5.2 ± 0.2	/	5.2 ± 0.2	3×10^{-4}
After 10 CV scans	$R_e(R_1Q_1)Q_g$	16.2 ± 0.2	/	16.2 ± 0.2	1×10^{-4}

The LNCAM1000_12h is evaluated in Fig. 3 by galvanostatic cycling in lithium half-cell performed by increasing the charge voltage cutoff from 4.4 V (panels a, b) to 4.8 V (panels c, d) and to 4.9 (panels e, f) at the constant rate of C/20 (1C = 298 mA g^{-1}) in order to verify the effects of the irreversible oxidation on cell response and stability. As expected by the CV previously discussed in Fig. 2, the cycling test with voltage range restricted between 2.5 V and 4.4 V (Fig. 3a, b) shows at the first cycle (inset of Fig. 3a) only the single-step charge and discharge

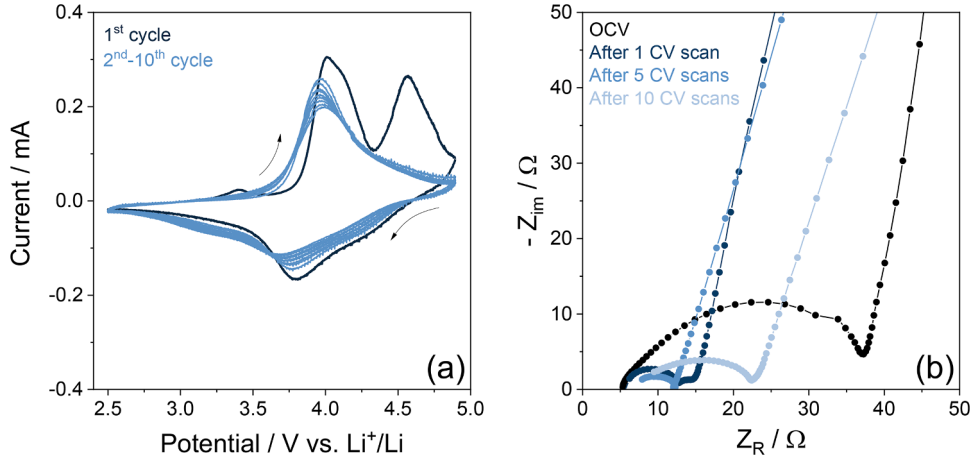

Fig. 2. **(a)** CV and **(b)** EIS measurements performed on the Li|EC:DMC 1:1 v/v 1 M $LiPF_6$|LNCAM1000_12h three-electrode cell using a Li reference electrode. CV potential range: 2.5 – 4.9 V *vs.* Li^+/Li; scan rate: 0.1 mV s^{-1}. EIS carried out at the OCV of the cell and after 1, 5 and 10 cycles; frequency range: 500 kHz – 100 mHz; alternate voltage signal: 10 mV. See the Experimental section for acronyms.

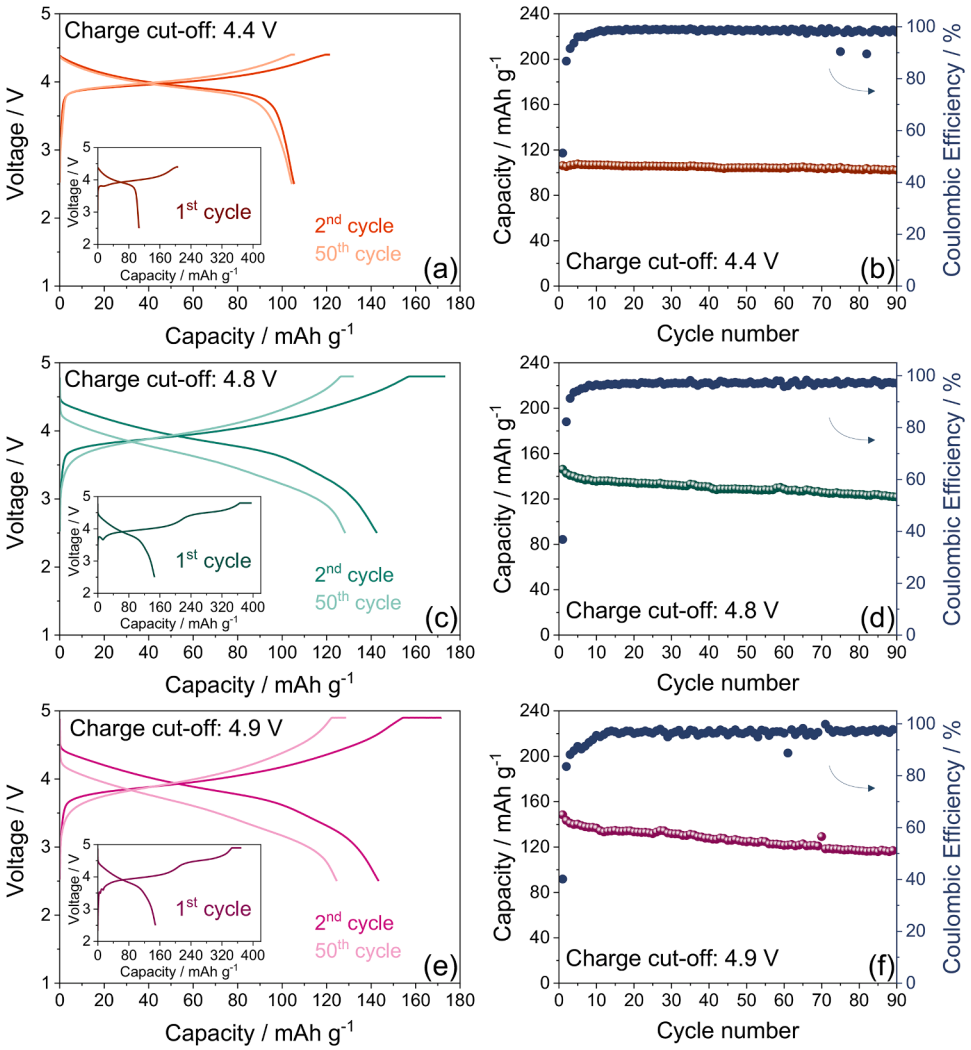

Fig. 3. Galvanostatic cycling performances of the Li|EC:DMC 1:1 v/v 1 M $LiPF_6$| LNCAM1000_12h cell at the constant current rate of C/20 (1C = 298 mA g^{-1}) in terms of **(a, c, e)** voltage profiles (insets show first cycle) and **(b, d, f)** discharge capacity trends reporting coulombic efficiency on right y-axes. Voltage ranges: **(a, b)** 2.5 – 4.4 V, **(c, d)** 2.5 – 4.8 V, and **(e, f)** 2.5 – 4.9 V. Measurements performed employing an additional constant voltage step at either 4.4 V, 4.8 V, or 4.9 V, respectively, held until a current value of ¼ of the nominal C-rate is reached (CCCV mode). Room temperature (25 °C). See the Experimental section for acronyms.

processes centered around 4.0 V ascribed to the Li^+ (de)intercalation process. On the other hand, the first cycle reveals a remarkably higher charge specific capacity (207 mAh g^{-1}) compared to discharge (106 mAh g^{-1}) due to the above mentioned cathode structural rearrangement and partial electrolyte decomposition which appear affecting the cell even with a charge cutoff limited to 4.4 V. The subsequent cycles in Fig. 3a reveal a highly reversible charge/discharge process, which is confirmed by the cycling trend in Fig. 3b with a stable discharge capacity of 106 mAh g^{-1} retained for over 96% at the end of the test, and a coulombic efficiency raising from 50% at the first cycle over 98% at the steady state. Despite the stability, the specific capacity delivered by LNCAM1000_12h in the 2.5 – 4.4 V voltage range barely exceeds 1/3 of the theoretical value (298 mAh g^{-1}), which may possibly limit its practical application in fields in which high energy density is requested [69,70]. The cycling tests performed by using the wider voltage ranges of 2.5 – 4.8 V (Fig. 3c, d) and 2.5 – 4.9 V (Fig. 3e, f) show during the first cycle (insets in Fig. 3c and e, respectively) irreversible oxidation processes leading to charge capacity values of 397 mAh g^{-1} at 4.8 V (Fig. 3c) and 370 mAh g^{-1} at 4.9 V (Fig. 3e), reflected into respective discharge capacities of 146 mAh g^{-1} and 148 mAh g^{-1}; this behavior confirms the irreversibility evidenced in CV profiles (see Fig. 2a). The slightly higher capacity observed at the first cycle charging process in the 2.5 – 4.8 V voltage range (397 mAh g^{-1}) in comparison with the 2.5 – 4.9 V voltage range (370 mAh g^{-1}) is related to the irreversible oxidation process ascribed to electrolyte with partial oxygen loss from cathode [63]. This process may be also affected by the amount of the active material in the electrode, particularly affecting the electrolyte oxidation, which may slightly differ in the various samples taken into account. In spite of the excessive oxidation capacity observed during the first cycle, the cells of Fig. 3c and e surprisingly exhibit the typical sloped profiles centered at 3.9 V, a discharge capacity approaching 150 mAh g^{-1}, and a well improved reversibility during the subsequent cycles. On the other hand, the increase of the charge cutoff from 4.8 V to 4.9 V clearly affects the capacity decay of the cell, as evidenced by the cycling trends reported in Fig. 3d and f, respectively. This behavior may be related to charge compensation of the irreversible oxygen loss and possible Ni reduction process at the first cycle accompanied by hysteresis [16]. Indeed, the cell cycled between 2.5 V and 4.8 V shows a capacity retention of 83% and a coulombic efficiency that increases from 37% at the first cycle to about 98% at the end of the test, while the cell tested between 2.5 V and 4.9 V reveals a retention of 77% and initial coulombic efficiency of 40% raising to 98% at the end of the test. Considering the comparable delivered capacity and the better retention achieved by adopting the 2.5 – 4.8 V voltage range compared to 2.5 – 4.9 V, the former is considered a suitable compromise to achieve satisfactory energy and stability which are key factors for the successful application of the layered oxide cathode in lithium-ion batteries [39]. In addition, the relevant side oxidation of the first cycle (efficiency ~ 40%) that usually represents a severe issue for battery application may be exploited to compensate the typical irreversibility affecting the Li-alloy materials as will be demonstrated hereafter. It is worth mentioning that the LNCAM1000_12h delivers a capacity ranging from 110 to 150 mAh g^{-1},

depending on the voltage cutoff, which is actually lower than the one delivered by commercial NMC (typically of about 190 mAh g^{-1}). The lower capacity value is ascribed to the inert Al used for stabilizing the P3-type structure [25], and the Jahn-Teller distortion attributed to the high amount of Mn instead of Co in the electrode formulation [71]. Despite the lower capacity, the substitution of the toxic and expensive Co with Al and Mn leads to notable reduction of the economical and environmental impact of the electrode.

Prior to further testing in cell, the effects on the layered structure of the severe irreversibility affecting LNCAM1000_12h at high voltage are investigated by performing *ex-situ* XRD on electrodes retrieved from lithium cells after 1 and 2 cycles at C/20 between 2.5 and 4.9 V. Fig. 4 displays the comparison between the XRD of pristine and cycled LNCAM1000_12h electrodes in the 10 – 60° range (Fig. 4a), and provides additional focus of the (003) plane in the 17 – 20° 2θ region (Fig. 4b) and the (104) reflection between 43° and 46° (Fig. 4c). Fig. 4a confirms the retention of the layered structures in the cycled electrodes (*R*-3*m* space group, table n. 166 [25]) which show the same diffraction peaks, along with a broad and weak signal extending from about 15° to 30° ascribed to the conducting carbon fraction in the electrode composition (see Experimental section). This experimental result justifies the evolution of the characteristic (de)intercalation profile of the layered cathode even upon the first cycle irreversibility as well as the relevant cell stability. Interestingly, the magnification of the 17 – 20° 2θ region in Fig. 4b reveals the shift of the (003) plane from 18.68° at the pristine condition to 18.54° after 1 charge/discharge cycle and then to 18.74° after 2 cycles in lithium cell (see peak indexing in Figure S2 in Supplementary Material). A similar trend can be observed for the (104) reflection in the magnified 43 – 46° 2θ region in Fig. 4c, which moves from 44.58° at the pristine state to 44.50° and to 44.70° upon 1 and 2 cycles, respectively. The shift of the (003) and (104) reflections well supports the above mentioned structural variation for the LNCAM1000_12h material upon cycling in lithium cell with possible partial oxygen loss and aluminum insertion defective sites [25,70,72]. However, a contribution to the cell irreversible capacity of the side reaction with the electrolyte leading to the SEI layer formation at the electrode/electrolyte interphase cannot be neglected [73].

The cycling performance of the LNCAM1000_12 h at higher current rates is also evaluated by additional galvanostatic charge/discharge measurements within the optimal 2.5 – 4.8 V voltage range. Figure S4 in the Supplementary Material shows a test performed on a Li|LNCAM1000_12h cell at C-rate increasing from C/10 to C/8, C/5, C/3 and 1C. Selected voltage profiles (Figure S4a) display the single-step charge/discharge reversible process already observed in Fig. 3, with increasing polarization from C/10 to 1C as expected by the ohmic drop promoted by the current increase. The corresponding cycling trend in Figure S4b reveals an initial discharge capacity of 134 mAh g^{-1} at C/10 which stabilizes at 117 mAh g^{-1} after 5 cycles, and values of 109, 96, 80 and 46 mAh g^{-1} at C/8, C/5, C/3 and 1C, respectively. Lowering back the C-rate to C/10 after 25 cycles leads to a capacity of about 110 mAh g^{-1}, that is, the 82% of the initial value, which suggests a moderate stability of the LNCAM1000_12h upon the stress triggered by the progressive raise of the current [53]. Prolonged galvanostatic cycling tests are reported in Fig. 5 to determine the cycle life of the LNCAM1000_12h material at constant C-rates of C/10 (Fig. 5a, b) and C/5 (Fig. 5c, d). Both cells show the expected irreversible double-plateau during charge at the first cycle (insets in Fig. 5a and c), and exclusively the reversible Li^+ (de) intercalation in the subsequent cycles (Fig. 5a, c) with more remarkable slope compared to the tests at C/20 (see Fig. 3), due to the higher currents [74]. Maximum discharge capacities of 137 mAh g^{-1} and 129 mAh g^{-1} are respectively achieved at C/10 (Fig. 5b) and C/5 (Fig. 5d), retained over 73% and 66% after 100 cycles. As expected, low coulombic efficiency of about 50% is achieved both at C/10 and C/5 during the first cycle, which subsequently increases and reach values of 98% and 99%, respectively, at the end of the test. The promising performance exhibited by the LNCAM1000_12h cathode may be possibly improved upon optimization of the synthesis process in order to enhance the stability of the layered structure, mitigate the irreversible oxidation process, and limit the capacity decay.

As previously mentioned, the initial relevant irreversibility of the cathode can be potentially exploited to compensate similar side processes occurring during the first discharge of lithium-alloying anodes such as silicon or tin, which are typically promoted by excessive volume changes, electrolyte reduction, and partial lithiation of the electrode matrix [75]. Indeed, pre-activation processes including direct contact with lithium metal (chemical strategy [30]) and/or preliminary cycling in lithium half-cell (electrochemical strategy [44]) are usually necessary prior to application in full Li-ion cell, in order to prevent parasitic reactions that would compromise the anode/cathode balancing. However, these efficient pre-activation procedures are still within a R&D stage mainly adopted for laboratory prototype cells [43,76,77]. Herein we avoid additional processes and directly combine a silicon oxide anode coated by 70% (w:w) of carbon, as indicated by TGA in Figure S5 in the Supplementary Material [27], with the developed layered cathode in a full Li-ion cell by advantageously tuning the negative to positive (N/P) ratio estimated from the respective irreversible capacity. The N/P ratios were calculated taking into account mass loadings and specific capacities of the two electrodes at the first charge of a full-cell including the irreversible part, that is, 300 mAh g^{-1} for first cathode de-lithiation and 810 mAh g^{-1} for first anode lithiation (see Experimental Section for further details). As reported in Fig. 6, a higher cathode content doesn't lead to lithium deposition, which is instead expected at much lower potential. Rather, the excess of cathode causes the irreversible electrolyte reduction at the anode side during the first cycle of the full cell with

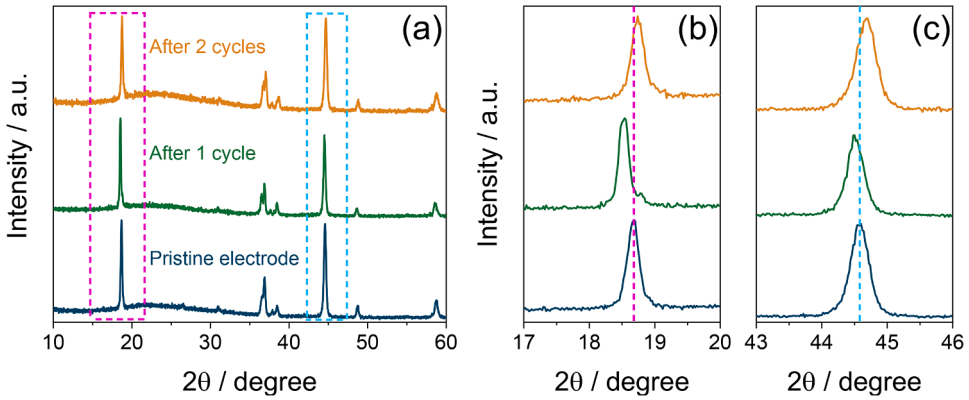

Fig. 4. **(a)** XRD patterns of the LNCAM1000_12h electrode at the pristine state and after 1 and 2 charge/discharge cycles in lithium cell at the constant current rate of C/20 (1C = 298 mA g^{-1}) between 2.5 and 4.9 V, with an additional constant voltage step at 4.9 V held until a current value of ¼ of the nominal C-rate is reached (CCCV mode). **(b, c)** Magnification of the **(b)** 17 – 20° and **(c)** 43 – 46° 2θ regions. See Experimental section for acronyms.

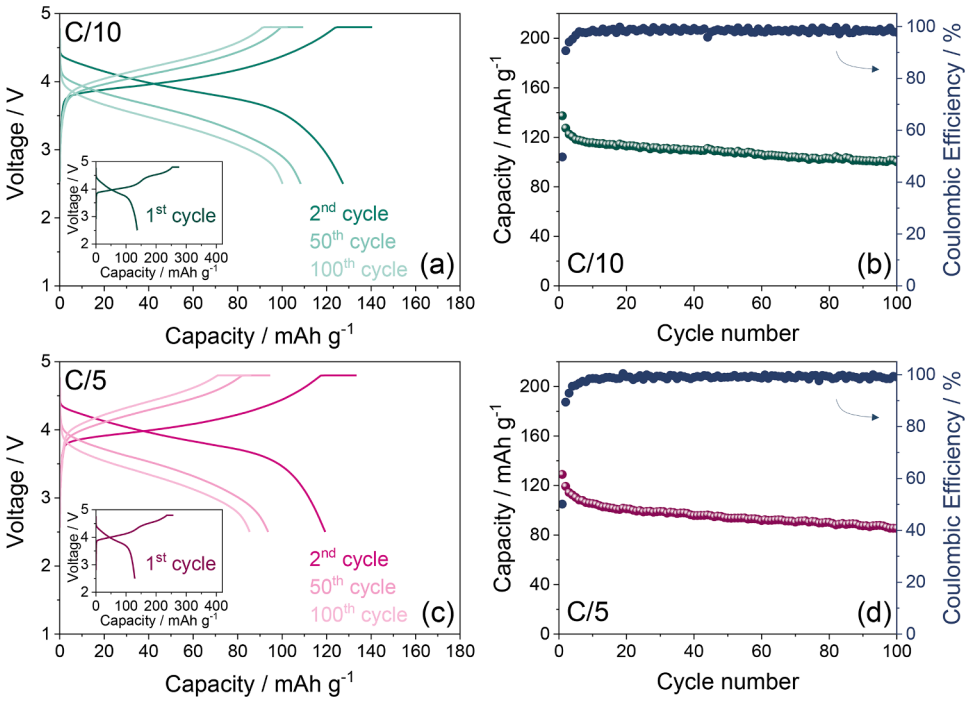

Fig. 5. Galvanostatic cycling performances of the Li|EC:DMC 1:1 v/v 1 M $LiPF_6$| LNCAM1000_12h cell at the constant current rate of **(a, b)** C/10 and **(c, d)** C/5, (1C = 298 mA g^{-1}) in terms of **(a, c)** voltage profiles (insets show first cycle) and **(b, d)** discharge capacity trend reporting coulombic efficiency on right y-axes. Voltage range: 2.5 – 4.8 V. Measurements performed with an additional constant voltage step at 4.8 V held until a current value of ¼ of the nominal C-rate was reached (CCCV mode). Room temperature (25 °C). See the Experimental section for acronyms.

formation of a stable SEI, and holds the alloying material at sufficiently low potential to allow battery operation during the subsequent cycles. Fig. 6 depicts the electrochemical behavior of two SiO_x-C|LNCAM1000_12h full-cells cycled at the constant current of C/10 as referred to the cathode (1C = 298 mA $g^{-1}_{cathode}$) using N/P ratio of either 0.98 or 0.84 calculated as indicated above. The cell response is reported in terms of the voltage trend *vs.* time of the full-cells (Fig. 6a and b for N/P of 0.98 and 0.84, respectively) as well as of the signals of the cathode (Fig. 6c and d) and the anode (Fig. 6e and f), which are concomitantly recorded using an additional lithium electrode as reference (see Experimental section). The measurement clearly exhibits for the SiO_x-C|LNCAM1000_12h full-cells (Fig. 6a, b) voltage profiles reflecting the combination of the respective cathode (Fig. 6c, d) and anode (Fig. 6e, f) signatures, and suggests a reciprocal compensation of irreversible capacities during the first charge, thus leading to a subsequent discharge fully in line with the one related to the Li|LNCAM1000_12h half-cell (compare voltage profiles of Fig. 6c, d with insets of Fig. 5a, c). Furthermore, the cathode side shows initial discharge capacity and cutoff remarkably depending on the N/P ratio with values of ~100 mAh g^{-1} at ~3.7 V in the cell using N/P of 0.98 (Fig. 6c), and ~115 mAh g^{-1} at ~3.5 V in the one using N/P of 0.84 (Fig. 6d). The charge/discharge profiles of the full-cell with N/P ratio of 0.98 (Fig. 6a) display more pronounced alteration. In fact, the working voltage of the electrodes is increased upon cycling more than the cell with N/P of 0.84 (Fig. 6b). This difference suggests a better reciprocal compensation of the irreversible capacity ascribed to LNCAM1000_12h (Fig. 6d) and SiO_x-C (Fig. 6f) through N/P of 0.84 compared to 0.98 (Fig. 6c and e, respectively). In detail, the LNCAM1000_12h cathode in the cell with N/P = 0.98 (Fig. 6c) delivers irreversible charge capacity of 338 mAh g^{-1} (1.12 mAh) at a final voltage cutoff of 4.971 V, while the cathode in the cell with N/P = 0.84 (Fig. 6d) displays a first charge capacity of 299 mAh g^{-1} (0.95 mAh) at 4.858 V cutoff. The respective SiO_x-C discharge capacities and voltage cutoff in the full-cell are of 933 mAh g^{-1} (1.12 mAh) at 0.170 V (N/P = 0.98, Fig. 6e) and 960 mAh g^{-1} (0.95 mAh) at 0.056 V (N/P = 0.84, Fig. 6f). Thus, as mentioned before, the results reveal that the use of a N/P ratio of 0.98 is insufficient to allow a full Li-alloying process of the anode during first charge of the corresponding Li-ion cell with consequent low utilization of SiO_x-C as indicated by the relatively high final reduction voltage (*i.e.*, 0.170 V). Instead, the lower anode content achieved by setting up a N/P of 0.84 increases the utilized fraction of the alloying material as indeed evidenced by the final voltage cutoff of the SiO_x-C (*i.e.*, 0.056 V) achieved by full-cell charge. The first discharge of the full-cell further supports the improvement achieved by setting up a N/P of 0.84 which leads to capacity of 113 mAh g^{-1} at 3.534 V cutoff for LNCAM1000_12h (Fig. 6d) and 364 mAh g^{-1} at 2.009 V for SiO_x-C (Fig. 6f) with respect to 97 mAh g^{-1} at 3.681 V and 275 mAh g^{-1} at 2.163 V, respectively, related to N/P of 0.98 (Fig. 6c, e).

Fig. 7 reports the cycling behavior of the above full SiO_x-C|LNCAM1000_12h cells in terms of gravimetric capacity calculated with respect to the active cathode mass (see Experimental section for details), delivered at C/10 with N/P ratio of either 0.98 (Fig. 7a, c) or 0.84 (Fig. 7b, d). The voltage profiles related to the cell with N/P = 0.98 (Fig. 7a) show a higher irreversible charge capacity at the first cycle compared to the cell with N/P = 0.84 (Fig. 7b), that is, 279 mAh g^{-1} and 258 mAh g^{-1}, respectively, reflected in subsequent discharge capacity of 99 mAh g^{-1} and 115 mAh g^{-1} and corresponding coulombic efficiency of 35% and 44%. Moreover, the cell with N/P ratio of 0.98 shows a more relevant capacity loss with a value of 60 mAh g^{-1} upon 10 cycles and lower final coulombic efficiency of 76% compared to the cell with N/P ratio of 0.84 that delivers a capacity of 73 mAh g^{-1} and coulombic efficiency of 87% at the end of the test. The voltage profiles displayed in Fig. 7 show a polarization resulting from the combination of the sloped behavior of anode and cathode, as already mentioned in Fig. 6, thus suggesting an effective reciprocal compensation of the irreversible capacity at the first cycle despite a further effort is be required to fully optimize the cell. These data confirm once more a better utilization of LNCAM1000_12h and SiO_x-C by setting up a N/P of 0.84 in agreement with the performance of the single electrodes discussed in Fig. 6. To further investigate the cycling behavior of the SiO_x-C|LNCAM1000_12h system, a coin-type full cell with N/P of 0.91 was tested and the results are shown in Figure S6 in the Supplementary Material. The cell shows high irreversible charge capacity at the first cycle, that is 294 mAh g^{-1}, and discharge capacity of 104 mAh g^{-1}, with corresponding coulombic efficiency of 35%. Subsequently, the cell delivers a capacity of about 80 mAh g^{-1} during the initial cycling stages, which stabilizes at about 70

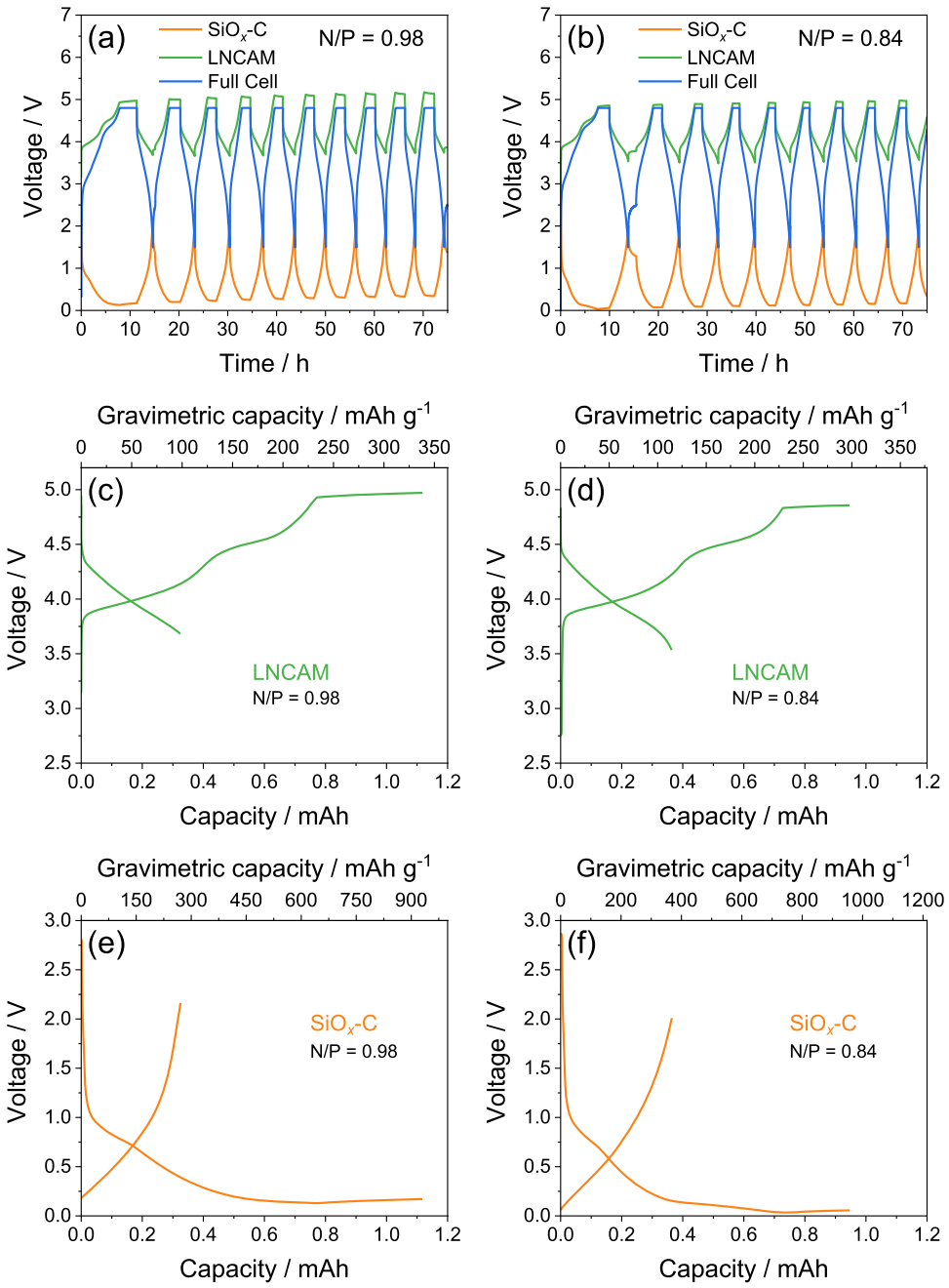

Fig. 6. (a, b) Time evolution of the SiO_x-C anodes and the LNCAM1000_12h cathodes voltage concomitantly collected by using an additional Li electrode as reference, and of the corresponding SiO_x-C|EC:DMC 1:1 v/v 1 M $LiPF_6$|LNCAM1000_12h full-cells cycled at C/10 (1C = 298 mA g^{-1}) with N/P ratio of either **(a)** 0.98 or **(b)** 0.84; panels **(c-f)** show the first cycle in terms of voltage *vs.* capacity (mAh, bottom x-axes) and gravimetric capacity (mAh g^{-1}, top x-axes) related to **(c, d)** LNCAM1000_12h cathodes and **(e, f)** SiO_x-C anodes in the full-cells with N/P ratio of either **(c, e)** 0.98 or **(d, f)** 0.84. Voltage range: 1.5 – 4.8 V. Measurements performed with an additional constant voltage step at 4.8 V held until a current value of ¼ of the nominal C-rate was reached (CCCV mode). Room temperature (25 °C). See the Experimental section for acronyms.

mAh g^{-1} after 20 cycles retained until the end of the test, with a coulombic efficiency approaching 85%. Therefore, the excess of the cathode in the SiO_x-C|LNCAM1000_12h cell may represent a viable strategy to improve the cycling behavior. In fact, the cell with a N/P ratio of 0.91 delivers capacity and efficiency values close to the ones obtained for the cell with N/P with 0.84 (Fig. 7b, d). These data suggest the need of further optimization of the electrode balancing to achieve a higher capacity [57]. Moreover, a capacity retention of about 70% after 50 charge/discharge cycles could represent a promising result in terms of stability of the cell, despite enhanced synthesis pathway for the LNCAM material and optimized cell may lead to performance of practical interest [33,57,78].

On the other, hand we focus herein on a proof-of-concept Li-ion battery combining electrode materials without any pre-treatment or activation process to overcome one the main critical issues that avoids the large scale diffusion of these appealing energy storage systems.

With the aim of further investigating the effects of the selected N/P ratio, a detailed study of the electrode/electrolyte interphase is performed on the SiO_x-C|LNCAM1000_12h cells by carrying out EIS at OCV and at full discharged states after few galvanostatic cycles, as reported in Fig. 8. The use of an additional lithium electrode as reference in the cells allows the study of three different sides of each cell, that is, SiO_x-C *vs.* Li (Fig. 8a, b), LNCAM1000_12h *vs.* Li (Fig. 8c, d) and SiO_x-C *vs.* LNCAM1000_12h (Fig. 8e, f) at OCV condition as well as after 1 and 10 charge/discharge cycles. The NLLS analyses performed on the Nyquist plots of Fig. 8 displayed in Table 4 reveal that all the considered systems can be generally represented by the $R_e(R_iQ_i)Q$ circuit, where R_e is the electrolyte resistance, R_i and Q_i account for the electrode/electrolyte interphase, and Q is a constant phase element that may refer to the cell geometric capacitance or to the Warburg-type Li^+ ions diffusion, depending on the system taken into account [48,49]. It is worth mentioning that Table 4 reports the overall resistance (R_e+R_i) instead of

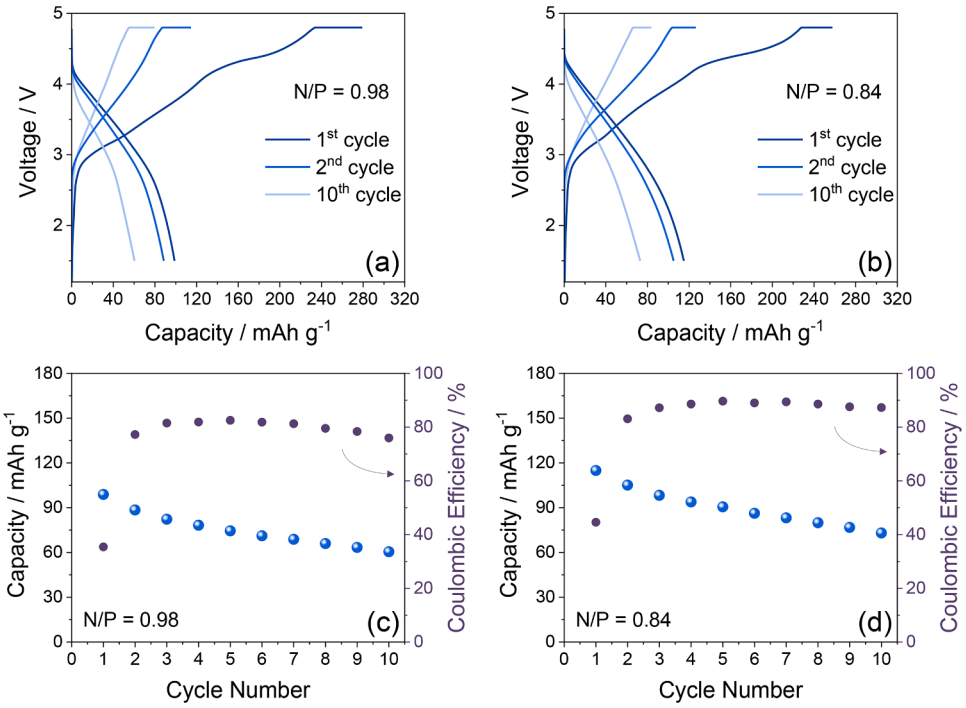

Fig. 7. (a, b) Voltage profiles and **(c, d)** capacity trends (right y-axes show coulombic efficiency) of the SiO_x-C|EC:DMC 1:1 v/v 1 M $LiPF_6$|LNCAM1000_12h full-cells with N/P ratio of either **(a, c)** 0.98 or **(b, d)** 0.84 cycled at the constant current rate of C/10 (1C = 298 mA g^{-1}). Cells assembled with an additional Li electroe as reference. Voltage range: 1.5 – 4.8 V. Measurements performed with an additional constant voltage step at 4.8 V held until a current value of ¼ of the nominal C-rate was reached (CCCV mode). Room temperature (25 °C). See the Experimental section for acronyms.

the single values to avoid differences ascribed to the cell geometry in the various configurations, in particular those referring to the third Li electrode. In fact, the latter cell setup involves a larger amount of electrolyte between electrodes and Li-reference and typically higher resistances compared to a Li-ion cell closely stacking the SiO_x-C anode and the LNCAM1000_12h cathode (see Experimental section for details). Indeed, the full-cell with N/P ratio of 0.98 exhibits a resistance value referred to the SiO_x-C/Li system (Fig. 8a) around 458 Ω at the OCV condition, that greatly increases to 8259 Ω upon 10 cycles (inset of Fig. 8a). A similar trend is observed for the LNCAM1000_12h/Li system of the same cell (Fig. 8c) with initial resistance of 399 Ω, that reaches after 10 cycles a value of 7246 Ω (inset of Fig. 8c). On the other hand, the full-cell assembled with N/P = 0.84 presents at the OCV condition a resistance of 268 Ω for the SiO_x-C/Li system (Fig. 8b) and 345 Ω for LNCAM1000_12h/Li (Fig. 8d) that increase after 10 cycles to 5467 Ω (inset of Fig. 8b) and 8282 Ω (inset of Fig. 8d). Hence, the cell with N/P of 0.84 shows a much lower increase of the anodic side resistance compared to the cell with N/P of 0.98, and a slightly higher increase of the cathodic side value by cycling, thus suggesting a mitigated degradation of the SiO_x-C anode interphase in the former cell compared to the latter, and a substantial similarity of the LNCAM1000_12h cathode interphase. On the other hand, the SiO_x-C/LNCAM1000_12h cells with N/P = 0.98 (Fig. 8e) and N/P = 0.84 (Fig. 8f) display resistance values two order of magnitude lower compared to the corresponding anode/-cathode *vs.* third Li electrode systems due to the above mentioned geometry differences. Despite the similarity, the full-cell with N/P ratio of 0.98 reveals slightly higher resistances compared to the one with N/P of 0.84, with values increasing from 8.3 Ω at the OCV to 13.7 Ω in the former and from 7.5 Ω at the OCV to 12.2 Ω in the latter, which is in line with the combined trend of the corresponding electrodes referred to the additional lithium electrode. Hence, the study of the SiO_x-C or LNCAM1000_12h electrodes using the Li reference gives additional insights on the electrode/electrolyte interphases of cathode and anode which are not fully revealed by considering the combination of the two materials in a full Li-ion cell. In general, the NLLS analyses suggest that the rapid capacity decay observed in Fig. 7a for the full-cell using N/P ratio of 0.98 is mainly related with the excessive increase of the SiO_x-C interphase resistance possibly due to the electrolyte degradation promoted by the voltage change during operation [79]. Instead, the full-cell with N/P ratio of 0.84 allows a limited increase of the SiO_x-C interphase resistance, despite the limited increase of the value ascribed to the LNCAM1000_12h cathode which appears to have less effect on the cell decay. Interestingly, the two Li-ion cells have similar resistance values, whilst substantial differences between the anode and cathode detected by the Li reference suggest a controlling role of the anode, and a better electrode/electrolyte interphase using N/P of 0.84 reflected into a better cycling performance [80].

Conclusions

We reported herein the synthesis and characterization of a $LiNi_{0.2}Co_{0.2}Al_{0.1}Mn_{0.45}O_2$ layered oxide cathode material as well as its application in a Li-ion cell using a SiO_x-C alloying anode without any pre-activation processe. SEM performed on the cathode revealed stacked submicrometric flakes forming layered micrometric particles, while EDS images suggested homogeneous distribution of the elements and a stoichiometry close to the expected one, validated by ICP-MS. XRD refinement confirmed the formation of the P3-type layered structure with trigonal cell unit (hexagonal *R*-3*m* space group, table n. 166), supported by Raman spectroscopy that showed the corresponding M–O bonds vibration. The investigation of the electrochemical process in lithium half-cell by CV revealed an irreversible oxidation process during the first cycle centered at 4.6 V *vs.* Li^+/Li due to structural rearrangement with partial oxygen loss and SEI formation upon electrolyte oxidation. The subsequent voltammetry cycles indicated the exclusive presence of the single-step reversible Li^+ (de)intercalation process occurring between 3.7 and 3.9 V *vs.* Li^+/Li with low polarization. EIS measurements carried out upon CV suggested the formation of a suitable electrode/electrolyte interphase with resistance value decreasing from 32 Ω at the OCV condition to 16 Ω at the end of the test. Galvanostatic cycling performed in lithium half-cells using the layered cathode at the constant current rate of C/20 (1C = 298 mA g^{-1}) indicated the 2.5 – 4.8 V voltage range as the most adequate operative condition to achieve fair compromise between delivered capacity (150 mAh g^{-1}), retention (83% at the end of the test) and coulombic efficiency (98% upon initial cycles). The effect of the cycling tests on the layered structure was

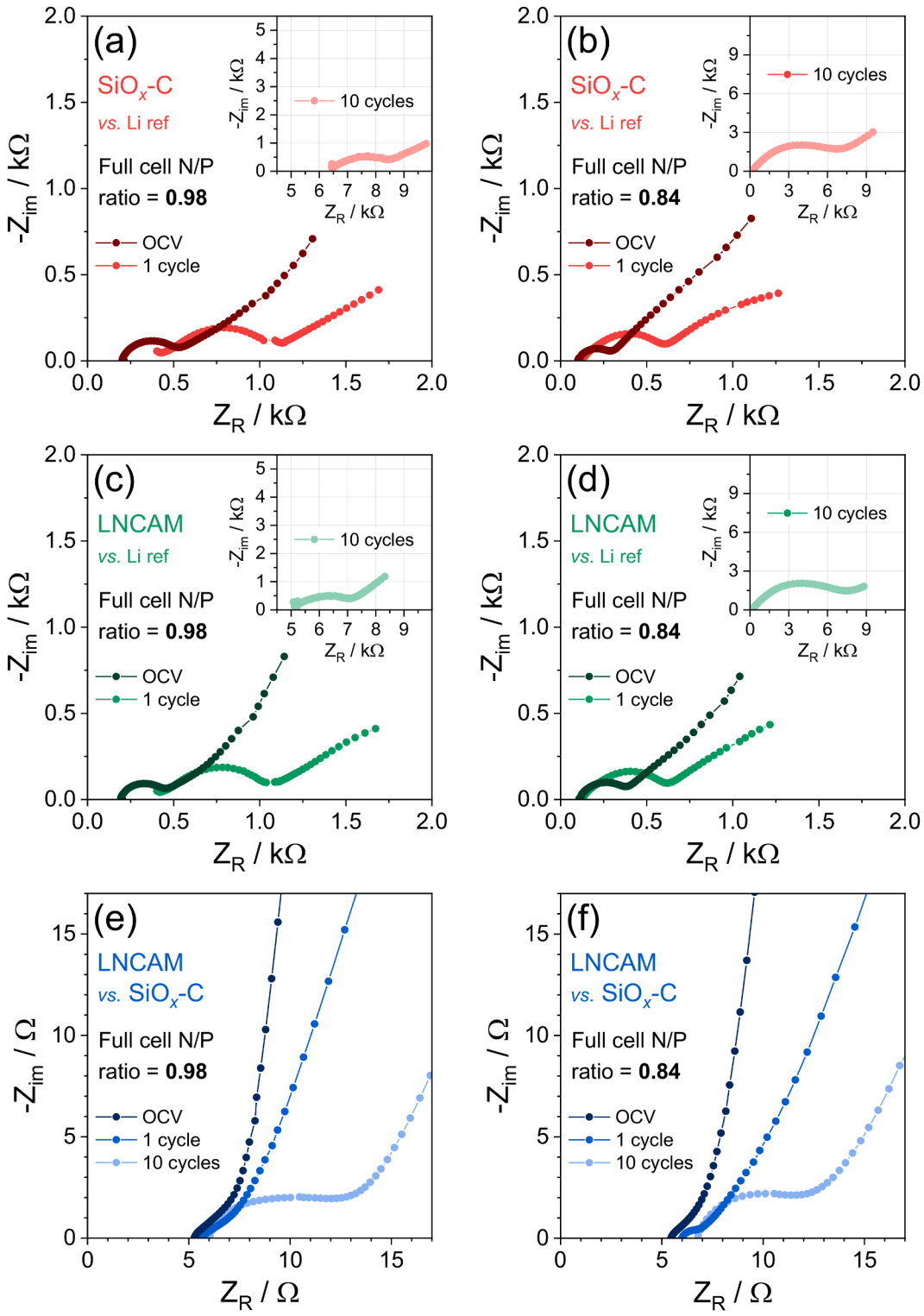

Fig. 8. EIS measurements performed on SiO_x-C|EC:DMC 1:1 v/v 1 M $LiPF_6$|LNCAM1000_12h full-cells. In detail: Nyquist plots related to the **(a, b)** SiO_x-C anode and **(c, d)** LNCAM1000_12h cathode collected concomitantly by using an additional Li electrode as reference in **(e, f)** full-cells with N/P ratio of either **(a, c, e)** 0.98 or **(b, d, f)** 0.84; EIS carried out at the OCV of the cells and after 1 and 10 galvanostatic cycles (insets) depicted in Figures 6 an 7; frequency range 500 kHz – 100 mHz; alternate voltage signal: 30 mV. See the Experimental section for acronyms.

investigated by *ex-situ* XRD upon charge/discharge cycles at C/20 in lithium half-cell. The diffractograms revealed the shift of the (003) and (104) main reflections related to the LNCAM structure to lower 2θ upon 1 cycle and to higher angles after 2 cycles due to the occurring of the structural modifications already suggested by CV. Additional charge/discharge tests in half-cell at the constant rates of C/10 and C/5 between 2.5 and 4.8 V, performed to evaluate the cycling behavior of the cathode at higher current, revealed a capacity of 137 mAh g^{-1} retained at the 73% at C/10 and respective values of 129 mAh g^{-1} and 66% at C/5. The $LiNi_{0.2}Co_{0.2}Al_{0.1}Mn_{0.45}O_2$ cathode has been subsequently coupled with the SiO_x-C alloying anode in proof-of-concept Li-ion cells without any pre-activation process. The cells exploited a N/P ratio of either 0.98 or

Table 4
NLLS analyses of the Nyquist plots reported in Fig. 8 recorded by performing EIS on SiO_x-C|LNCAM1000_12h full-cells using an additional lithium electrode as reference and N/P ratio of either 0.98 or 0.84. The measurements were performed on three different sides of each cell, that is, SiO_x-C *vs.* Li reference, LNCAM1000_12h *vs.* Li reference and SiO_x-C *vs.* LNCAM1000_12h. NLLS analyses were performed through the Boukamp software and only fits with a χ^2 value of the order of 10^{-4} or lower were considered suitable [48,49]. See Experimental section for acronyms.

N/P ratio	Considered system	Cell condition	Circuit	$R_e + R_i$ [Ω]	χ^2
0.98	SiO_x-C *vs.* Li reference	OCV	$R_e(R_iQ_i)$ Q	458 ± 4	3×10^{-5}
		1 cycle	$R_e(R_iQ_i)$ Q	1103 ± 22	3×10^{-4}
		10 cycles	$R_e(R_iQ_i)$ Q	8259 ± 101	1×10^{-5}
	LNCAM1000_12h *vs.* Li reference	OCV	$R_e(R_iQ_i)$ Q	399 ± 8	2×10^{-4}
		1 cycle	$R_e(R_iQ_i)$ Q	1044 ± 14	1×10^{-4}
		10 cycles	$R_e(R_iQ_i)$ Q	7246 ± 57	1×10^{-5}
	LNCAM1000_12h *vs.* SiO_x-C	OCV	$R_e(R_iQ_i)$ Q	8.3 ± 0.2	4×10^{-5}
		1 cycle	$R_e(R_iQ_i)$ Q	8.5 ± 0.3	3×10^{-5}
		10 cycles	$R_e(R_iQ_i)$ Q	13.7 ± 0.3	2×10^{-4}
0.84	SiO_x-C *vs.* Li reference	OCV	$R_e(R_iQ_i)$ Q	268 ± 4	2×10^{-4}
		1 cycle	$R_e(R_iQ_i)$ Q	594 ± 15	3×10^{-4}
		10 cycles	$R_e(R_iQ_i)$ Q	5467 ± 150	1×10^{-4}
	LNCAM1000_12h *vs.* Li reference	OCV	$R_e(R_iQ_i)$ Q	345 ± 5	1×10^{-4}
		1 cycle	$R_e(R_iQ_i)$ Q	582 ± 14	4×10^{-4}
		10 cycles	$R_e(R_iQ_i)$ Q	8282 ± 74	2×10^{-4}
	LNCAM1000_12h *vs.* SiO_x-C	OCV	$R_e(R_iQ_i)$ Q	7.5 ± 0.2	4×10^{-5}
		1 cycle	$R_e(R_iQ_i)$ Q	6.7 ± 0.1	4×10^{-5}
		10 cycles	$R_e(R_iQ_i)$ Q	12.2 ± 0.3	2×10^{-4}

0.84, tuned by taking into account the characteristic initial irreversibility affecting both the layered cathode and the silicon oxide anode. Galvanostatic cycling tests performed on the full-cells at the constant current of C/10 (1C = 298 mA $g_{cathode}^{-1}$) have shown excessive degradation during the first charge for the cell with N/P = 0.98, leading to relevant increase of the voltage of both the electrodes and fast capacity decay. On the other hand, the cell using N/P ratio of 0.84 demonstrated a better cycling stability with a maximum delivered capacity of 115 mAh g^{-1}, retention of 63%, and final coulombic efficiency of 87%. The use of additional Li electrode as reference in the full-cells allowed the EIS investigation of cathode and anode interphases, as well as the monitoring of the full-cell behavior. The study indicated a strong influence of the Li-ion cell balancing on the electrode/electrolyte interphase characteristics, and suggested substantial differences between the anode and cathode resistance trends. In particular, the EIS revealed the controlling role of the anode, and a better electrode/electrolyte interphase and cycling performance for the cell using a cathode excess adopting a N/P of 0.84 compared to the one with N/P of 0.98. In summary, the tests demonstrated that the direct combination of the $LiNi_{0.2}Co_{0.2}Al_{0.1}Mn_{0.45}O_2$ layered cathode and the SiO_x-C alloying anode without additional pre-treatments may be a viable strategy to achieve efficient Li-ion systems, despite a further investigation may be required to determine the optimal N/P ratio.

CRediT authorship contribution statement

Luca Minnetti: Investigation, Visualization, Formal analysis, Writing – original draft. **Vittorio Marangon:** Investigation, Visualization, Formal analysis, Writing – original draft. **Paolo Andreotti:** Investigation, Formal analysis. **Antunes Staffolani:** Investigation, Formal analysis. **Francesco Nobili:** Writing – review & editing, Supervision. **Jusef Hassoun:** Conceptualization, Writing – original draft, Writing – review & editing, Validation, Supervision, Project administration, Funding acquisition.

Declaration of Competing Interest

The authors declare the following financial interests/personal relationships which may be considered as potential competing interests

Data availability

Data will be made available on request.

Acknowledgments

The work was performed within the grant "Fondo di Ateneo per la Ricerca Locale (FAR) 2021", University of Ferrara, and the collaboration project "Accordo di Collaborazione Quadro 2015" between University of Ferrara (Department of Chemical and Pharmaceutical Sciences) and Sapienza University of Rome (Department of Chemistry). J.H. and V.M. thank the European Union's Horizon 2020 research and innovation program Graphene Flagship, grant agreement No 881603.

Supplementary material

Supplementary material associated with this article can be found, in the online version, at doi:10.1016/j.electacta.2023.142263.

References

[1] J. Neubauer, E. Wood, Thru-life impacts of driver aggression, climate, cabin thermal management, and battery thermal management on battery electric vehicle utility, J. Power Sources 259 (2014) 262–275, https://doi.org/10.1016/j.jpowsour.2014.02.083.
[2] O. Ellabban, H. Abu-Rub, F. Blaabjerg, Renewable energy resources: current status, future prospects and their enabling technology, Renew. Sustain. Energy Rev. 39 (2014) 748–764, https://doi.org/10.1016/j.rser.2014.07.113.
[3] B. Scrosati, J. Hassoun, Y.-K. Sun, Lithium-ion batteries. a look into the future, Energy Environ. Sci. 4 (2011) 3287, https://doi.org/10.1039/c1ee01388b.
[4] D. Larcher, J.M. Tarascon, Towards greener and more sustainable batteries for electrical energy storage, Nat. Chem. 7 (2015) 19–29, https://doi.org/10.1038/nchem.2085.
[5] D. Di Lecce, R. Verrelli, J. Hassoun, Lithium-ion batteries for sustainable energy storage: recent advances towards new cell configurations, Green Chem. 19 (2017) 3442–3467, https://doi.org/10.1039/c7gc01328k.
[6] J. Hassoun, P. Ochal, S. Panero, G. Mulas, C. Bonatto Minella, B. Scrosati, The effect of CoSn/$CoSn_2$ phase ratio on the electrochemical behaviour of $Sn_{40}Co_{40}C_{20}$ ternary alloy electrodes in lithium cells, J. Power Sources 180 (2008), https://doi.org/10.1016/j.jpowsour.2008.01.059.
[7] A. Varzi, K. Thanner, R. Scipioni, D. Di Lecce, J. Hassoun, S. Dörfler, H. Altheus, S. Kaskel, C. Prehal, S.A. Freunberger, Current status and future perspectives of lithium metal batteries, J. Power Sources 480 (2020), 228803, https://doi.org/10.1016/j.jpowsour.2020.228803.
[8] J. Li, X. Wang, J. Zhao, J. Chen, T. Jia, C. Cao, Porous lithium nickel cobalt manganese oxide hierarchical nanosheets as high rate capability cathodes for lithium ion batteries, J. Power Sources 307 (2016) 731–737, https://doi.org/10.1016/j.jpowsour.2016.01.050.
[9] P. Rozier, J.M. Tarascon, Review—Li-rich layered oxide cathodes for next-generation Li-ion batteries: chances and challenges, J. Electrochem. Soc. 162 (2015) A2490–A2499, https://doi.org/10.1149/2.0111514jes.
[10] H. Choi, A.R. Schuer, H. Moon, M. Kuenzel, S. Passerini, Investigating the particle size effect on the electrochemical performance and degradation of cobalt-free lithium-rich layered oxide $Li_{1.2}Ni_{0.2}Mn_{0.6}O_2$, Electrochim. Acta 430 (2022), 141047, https://doi.org/10.1016/j.electacta.2022.141047.
[11] Y.-K. Sun, A rising tide of Co-free chemistries for Li-ion batteries, ACS Energy Lett 7 (2022) 1774–1775, https://doi.org/10.1021/acsenergylett.2c00908.

[12] Z. Chen, D. Chao, J. Lin, Z. Shen, Recent progress in surface coating of layered $LiNi_xCo_yMn_zO_2$ for lithium-ion batteries, Mater. Res. Bull. 96 (2017) 491–502, https://doi.org/10.1016/j.materresbull.2017.05.021.

[13] Y. Xia, J. Zheng, C. Wang, M. Gu, Designing principle for Ni-rich cathode materials with high energy density for practical applications, Nano Energy 49 (2018) 434–452, https://doi.org/10.1016/j.nanoen.2018.04.062.

[14] W. Hua, B. Schwarz, R. Azmi, M. Müller, M.S. Dewi Darma, M. Knapp, A. Senyshyn, M. Heere, A. Missyul, L. Simonelli, J.R. Binder, S. Indris, H. Ehrenberg, Lithium-ion (de)intercalation mechanism in core-shell layered $Li(Ni,Co,Mn)O_2$ cathode materials, Nano Energy 78 (2020), 105231, https://doi.org/10.1016/j.nanoen.2020.105231.

[15] D. Huang, Y. Shi, A.P. Tornheim, J. Bareño, Z. Chen, Z. Zhang, A. Burrell, H. Luo, Nanoscale $LiNi_{0.5}Co_{0.2}Mn_{0.3}O_2$ cathode materials for lithium ion batteries via a polymer-assisted chemical solution method, Appl. Mater. Today 16 (2019) 342–350, https://doi.org/10.1016/j.apmt.2019.06.008.

[16] L. Fang, L. Zhou, M. Park, D. Han, G. Lee, S. Kang, S. Lee, M. Chen, Z. Hu, K. Zhang, K. Nam, Y. Kang, Hysteresis induced by incomplete cationic redox in Li-Rich 3d-transition-metal layered oxides cathodes, Adv. Sci. 9 (2022), 2201896, https://doi.org/10.1002/advs.202201896.

[17] X. Gao, H. Liu, H. Chen, Y. Mei, B. Wang, L. Fang, M. Chen, J. Chen, J. Gao, L. Ni, L. Yang, Y. Tian, W. Deng, R. Momen, W. Wei, L. Chen, G. Zou, H. Hou, Y.-M. Kang, X. Ji, Cationic-potential tuned biphasic layered cathodes for stable desodiation/sodiation, Sci. Bull. 67 (2022) 1589–1602, https://doi.org/10.1016/j.scib.2022.06.024.

[18] J. Zhang, J.-B. Kim, J. Zhang, G.-H. Lee, M. Chen, V.W. Lau, K. Zhang, S. Lee, C.-L. Chen, T.-Y. Jeon, Y.-W. Kwon, Y.-M. Kang, Regulating Pseudo-Jahn–Teller effect and superstructure in layered cathode materials for reversible alkali-ion intercalation, J. Am. Chem. Soc. 144 (2022) 7929–7938, https://doi.org/10.1021/jacs.2c02875.

[19] L. Yang, F. Ren, Q. Feng, G. Xu, X. Li, Y. Li, E. Zhao, J. Ma, S. Fan, Effect of Cu doping on the structural and electrochemical performance of $LiNi_{1/3}Co_{1/3}Mn_{1/3}O_2$ cathode materials, J. Electron. Mater. 47 (2018) 3996–4002, https://doi.org/10.1007/s11664-018-6284-8.

[20] S. Liu, Z. Dang, D. Liu, C. Zhang, T. Huang, A. Yu, Comparative studies of zirconium doping and coating on $LiNi_{0.6}Co_{0.2}Mn_{0.2}O_2$ cathode material at elevated temperatures, J. Power Sources 396 (2018) 288–296, https://doi.org/10.1016/j.jpowsour.2018.06.052.

[21] H. Darjazi, E. Gonzalo, B. Acebedo, R. Cid, M. Zarrabeitia, F. Bonilla, M.Á. Muñoz-Márquez, F. Nobili, Improving high-voltage cycling performance of nickel-rich NMC layered oxide cathodes for rechargeable lithium–ion batteries by Mg and Zr co-doping, Mater. Today Sustain. 20 (2022), 100236, https://doi.org/10.1016/j.mtsust.2022.100236.

[22] K. Sahni, M. Ashuri, Q. He, R. Sahore, I.D. Bloom, Y. Liu, J.A. Kaduk, L.L. Shaw, H_3PO_4 treatment to enhance the electrochemical properties of $Li(Ni_{1/3}Mn_{1/3}Co_{1/3})O_2$ and $Li(Ni_{0.5}Mn_{0.3}Co_{0.2})O_2$ cathodes, Electrochim. Acta 301 (2019) 8–22, https://doi.org/10.1016/j.electacta.2019.01.153.

[23] Z. Li, N.A. Chernova, J. Feng, S. Upreti, F. Omenya, M.S. Whittingham, Stability and rate capability of Al substituted lithium-rich high-manganese content oxide materials for Li-ion batteries, J. Electrochem. Soc. 159 (2011) A116–A120, https://doi.org/10.1149/2.044202jes.

[24] Y. Gao, W. Yuan, X. Dou, Improvement of the high-performance Al-doped $LiNi_{1/3}Co_{1/3}Mn_{1/3}O_2$ cathode material for new electro-optical conversion devices, Front. Phys. 9 (2021) 1–7, https://doi.org/10.3389/fphy.2021.731851.

[25] J.D. Wilcox, E.E. Rodriguez, M.M. Doeff, The impact of aluminum and iron substitution on the structure and electrochemistry of $Li(Ni_{0.4}Co_{0.2-y}M_yMn_{0.4})O_2$ materials, J. Electrochem. Soc. 156 (2009) A1011, https://doi.org/10.1149/1.3237100.

[26] M. Ge, C. Cao, G.M. Biesold, C.D. Sewell, S. Hao, J. Huang, W. Zhang, Y. Lai, Z. Lin, Recent advances in silicon-based electrodes: from fundamental research toward practical applications, Adv. Mater. 33 (2021), 2004577, https://doi.org/10.1002/adma.202004577.

[27] G.A. Elia, J. Hassoun, A SiO_x-based anode in a high-voltage lithium-ion battery, ChemElectroChem 4 (2017) 2164–2168, https://doi.org/10.1002/celc.201700316.

[28] L. Liu, F. Xie, J. Lyu, T. Zhao, T. Li, B.G. Choi, Tin-based anode materials with well-designed architectures for next-generation lithium-ion batteries, J. Power Sources 321 (2016) 11–35, https://doi.org/10.1016/j.jpowsour.2016.04.105.

[29] D. Di Lecce, R. Verrelli, J. Hassoun, New lithium ion batteries exploiting conversion/alloying anode and $LiFe_{0.25}Mn_{0.5}Co_{0.25}PO_4$olivine cathode, Electrochim. Acta 220 (2016) 384–390, https://doi.org/10.1016/j.electacta.2016.10.067.

[30] S. Brutti, J. Hassoun, B. Scrosati, C. Lin, H. Wu, H. Hsieh, A high power Sn-C/C-$LiFePO_4$ lithium ion battery, J. Power Sources 217 (2012) 72–76, https://doi.org/10.1016/j.jpowsour.2012.05.102.

[31] W. Luo, J.-J. Gaumet, L.-Q. Mai, Antimony-based intermetallic compounds for lithium-ion and sodium-ion batteries: synthesis, construction and application, Rare Metals 36 (2017) 321–338, https://doi.org/10.1007/s12598-017-0899-4.

[32] H. Woo, S. Wi, J. Kim, J. Kim, S. Lee, T. Hwang, J. Kang, J. Kim, K. Park, B. Gil, S. Nam, B. Park, Complementary surface modification by disordered carbon and reduced graphene oxide on SnO_2 hollow spheres as an anode for Li-ion battery, Carbon N Y 129 (2018) 342–348, https://doi.org/10.1016/j.carbon.2017.12.015.

[33] S. Levchenko, S. Wei, V. Marangon, J. Hassoun, A Li-ion battery using nanostructured Sn@C alloying anode and high-voltage $LiNi_{0.35}Cu_{0.1}Mn_{1.45}Al_{0.1}O_4$ spinel cathode, Energy Technol. 123 (2022), 2200725, https://doi.org/10.1002/ente.202200725.

[34] J. Ge, Q. Tang, H. Shen, F. Zhou, H. Zhou, W. Yang, J. Hong, B. Xu, J. Saddique, Controllable preparation of disproportionated SiOx/C sheets with 3D network as high-performance anode materials of lithium ion battery, Appl. Surf. Sci. 552 (2021), 149446, https://doi.org/10.1016/j.apsusc.2021.149446.

[35] H.-W. Yang, D.I. Lee, N. Kang, J.-K. Yoo, S.-T. Myung, J. Kim, S.-J. Kim, Highly enhancement of the SiO nanocomposite through Ti-doping and carbon-coating for high-performance Li-ion battery, J. Power Sources 400 (2018) 613–620, https://doi.org/10.1016/j.jpowsour.2018.08.065.

[36] L. Sbrascini, A. Staffolani, L. Bottoni, H. Darjazi, L. Minnetti, M. Minicucci, F. Nobili, Structural and interfacial characterization of a sustainable Si/hard carbon composite anode for lithium-ion batteries, ACS Appl. Mater. Interfaces (2022), https://doi.org/10.1021/acsami.2c07888.

[37] G. Carbonari, F. Maroni, S. Gabrielli, A. Staffolani, R. Tossici, A. Palmieri, F. Nobili, Synthesis and characterization of vanillin-templated Fe_2O_3 nanoparticles as a sustainable anode material for Li-ion batteries, ChemElectroChem 6 (2019) 1915–1920, https://doi.org/10.1002/celc.201900189.

[38] S. Wei, D. di Lecce, R. Brescia, G. Pugliese, P.R. Shearing, J. Hassoun, Electrochemical behavior of nanostructured NiO@C anode in a lithium-ion battery using $LiNi_{1/3}Co_{1/3}Mn_{1/3}O2$ cathode, J. Alloys Compd. 844 (2020), 155365, https://doi.org/10.1016/j.jallcom.2020.155365.

[39] D. Di Lecce, P. Andreotti, M. Boni, G. Gasparro, G. Rizzati, J.Y. Hwang, Y.K. Sun, J. Hassoun, Multiwalled carbon nanotubes anode in lithium-ion battery with $LiCoO_2$, $Li[Ni_{1/3}Co_{1/3}Mn_{1/3}]O_2$, and $LiFe_{1/4}Mn_{1/2}Co_{1/4}PO_4$ cathodes, ACS Sustain. Chem. Eng. 6 (2018) 3225–3232, https://doi.org/10.1021/acssuschemeng.7b03395.

[40] S. Fang, F. Wu, M. Zarrabeitia, M. Kuenzel, D. Roscher, X. Gao, J. Kim, G. Kim, S. Passerini, Enhancing the Interfacial Stability of High-Energy Si/graphite|| $LiNi_{0.88}Co_{0.09}Mn_{0.03}O_2$ batteries employing a dual-anion ionic liquid-based electrolyte, Batter Supercaps 5 (2022), e202200286, https://doi.org/10.1002/batt.202200286.

[41] Q. Li, Y. Wu, Z. Wang, H. Ming, W. Wang, D. Yin, L. Wang, H.N. Alshareef, J. Ming, Carbon nanotubes coupled with metal ion diffusion layers stabilize oxide conversion reactions in high-voltage lithium-ion batteries, ACS Appl. Mater. Interfaces 12 (2020) 16276–16285, https://doi.org/10.1021/acsami.9b22175.

[42] Y. Wu, L. Xie, X. He, L. Zhuo, L. Wang, J. Ming, Electrochemical activation, voltage decay and hysteresis of Li-rich layered cathode probed by various cobalt content, Electrochim. Acta 265 (2018) 115–120, https://doi.org/10.1016/j.electacta.2018.01.181.

[43] V. Marangon, C. Hernández-Rentero, M. Olivares-Marín, V. Gómez-Serrano, Á. Caballero, J. Morales, J. Hassoun, A stable high-capacity lithium-ion battery using a biomass-derived sulfur-carbon cathode and lithiated silicon anode, ChemSusChem 14 (2021) 3333–3343, https://doi.org/10.1002/cssc.202101069.

[44] M. Agostini, S. Brutti, J. Hassoun, High voltage Li-ion battery using exfoliated graphite/graphene nanosheets anode, ACS Appl. Mater. Interfaces 8 (2016) 10850–10857, https://doi.org/10.1021/acsami.6b01407.

[45] D. Di Lecce, D. Campanella, J. Hassoun, Insight on the enhanced reversibility of a multimetal layered oxide for sodium-ion battery, J. Phys. Chem. C 122 (2018) 23925–23933, https://doi.org/10.1021/acs.jpcc.8b07596.

[46] I. Hasa, S. Passerini, J. Hassoun, Toward high energy density cathode materials for sodium-ion batteries: investigating the beneficial effect of aluminum doping on the P2-type structure, J. Mater. Chem. A Mater. 5 (2017) 4467–4477, https://doi.org/10.1039/C6TA08667E.

[47] L. Lutterotti, Total pattern fitting for the combined size-strain-stress-texture determination in thin film diffraction, Nucl. Instrum. Methods Phys. Res. B 268 (2010) 334–340, https://doi.org/10.1016/j.nimb.2009.09.053.

[48] B. Boukamp, A package for impedance/admittance data analysis, Solid State Ion 18–19 (1986) 136–140, https://doi.org/10.1016/0167-2738(86)90100-1.

[49] B. Boukamp, A nonlinear least squares fit procedure for analysis of immittance data of electrochemical systems, Solid State Ion 20 (1986) 31–44, https://doi.org/10.1016/0167-2738(86)90031-7.

[50] V. Hebbar, M. Viji, A.K. Budumuru, S. Gautam, K.H. Chae, K. Balaji, N.T. Kalyana Sundaram, A.K. Subramani, C. Sudakar, Morphology and interconnected microstructure-driven high-rate capability of Li-rich layered oxide cathodes, ACS Appl. Mater. Interfaces 12 (2020) 32566–32577, https://doi.org/10.1021/acsami.0c05752.

[51] Y.-J. Gu, Q.-G. Zhang, Y.-B. Chen, H.-Q. Liu, J.-X. Ding, Y.-M. Wang, H.-F. Wang, L. Chen, M. Wang, S.-W. Fan, Q.-F. Zang, X.-L. Yang, Reduction of the lithium and nickel site substitution in $Li_{1+x}Ni_{0.5}Co_{0.2}Mn_{0.3}O_2$ with Li excess as a cathode electrode material for Li-ion batteries, J. Alloys Compd. 630 (2015) 316–322, https://doi.org/10.1016/j.jallcom.2014.12.235.

[52] M.D. Radin, S. Hy, M. Sina, C. Fang, H. Liu, J. Vinckeviciute, M. Zhang, M. S. Whittingham, Y.S. Meng, A. Van der Ven, Narrowing the gap between theoretical and practical capacities in Li-ion layered oxide cathode materials, Adv. Energy Mater. 7 (2017), 1602888, https://doi.org/10.1002/aenm.201602888.

[53] M. Zukalova, J. Prochazka, B. Pitna Laskova, A. Zukal, L. Kavan, Layered $LiNi_{1/3}Mn_{1/3}Co_{1/3}O_2$ (NMC) with optimized morphology for Li-ion batteries, ECS Trans. 87 (2018) 67–75, https://doi.org/10.1149/08701.0067ecst.

[54] M. Eilers-Rethwisch, M. Winter, F.M. Schappacher, Synthesis, electrochemical investigation and structural analysis of doped $Li[Ni_{0.6}Mn_{0.2}Co_{0.2-x}M_x]O_2$ (x = 0, 0.05; M = Al, Fe, Sn) cathode materials, J. Power Sources 387 (2018) 101–107, https://doi.org/10.1016/j.jpowsour.2018.02.080.

[55] L.B. Mccusker, R.B. Von Dreele, D.E. Cox, D. Louër, P. Scardi, Rietveld refinement guidelines, J. Appl. Crystallogr. 32 (1999) 36–50, https://doi.org/10.1107/S0021889898009856.

[56] H. Gupta, S.K. Singh, N. Srivastava, D. Meghnani, R.K. Tiwari, R. Mishra, A. Patel, A. Tiwari, A.L. Saroj, R.K. Singh, Improved high voltage performance of Li-ion

conducting coated Ni-rich NMC cathode materials for rechargeable Li battery, ACS Appl. Energy Mater. 4 (2021) 13878–13889, https://doi.org/10.1021/acsaem.1c02681.
[57] Ahmed.M. Hashem, Rasha.S. El-Tawil, M. Abutabl, Ali.E. Eid, Pristine and coated $LiNi_{1/3}Mn_{1/3}Co_{1/3}O_2$ as positive electrode materials for li-ion batteries, Res. Eng. Struct. Mater. 1 (2015) 81–97, https://doi.org/10.17515/resm2015.07en0315.
[58] D. Ren, Y. Yang, L. Shen, R. Zeng, H.D. Abruña, Ni-rich $LiNi_{0.88}Mn_{0.06}Co_{0.06}O_2$ cathode interwoven by carbon fiber with improved rate capability and stability, J. Power Sources 447 (2020) 6–10, https://doi.org/10.1016/j.jpowsour.2019.227344.
[59] K.S. Park, M.H. Cho, S.J. Jin, K.S. Nahm, Y.S. Hong, Effect of Li ion in transition metal sites on electrochemical behavior of layered lithium manganese oxides solid solutions, Solid State Ion 171 (2004) 141–146, https://doi.org/10.1016/j.ssi.2004.04.016.
[60] V. Sharova, A. Moretti, T. Diemant, A. Varzi, R.J. Behm, S. Passerini, Comparative study of imide-based Li salts as electrolyte additives for Li-ion batteries, J. Power Sources 375 (2018) 43–52, https://doi.org/10.1016/j.jpowsour.2017.11.045.
[61] J. Demeaux, M. Caillon-Caravanier, H. Galiano, D. Lemordant, B. Claude-Montigny, $LiNi_{0.4}Mn_{1.6}O_4$/electrolyte and carbon black/electrolyte high voltage interfaces: to evidence the chemical and electronic contributions of the solvent on the cathode-electrolyte interface formation, J. Electrochem. Soc. 159 (2012) A1880–A1890, https://doi.org/10.1149/2.052211jes.
[62] J. Kasnatscheew, B. Streipert, S. Röser, R. Wagner, I. Cekic Laskovic, M. Winter, Determining oxidative stability of battery electrolytes: validity of common electrochemical stability window (ESW) data and alternative strategies, Phys. Chem. Chem. Phys. 19 (2017) 16078–16086, https://doi.org/10.1039/C7CP03072J.
[63] G.A. Elia, J. Wang, D. Bresser, J. Li, B. Scrosati, S. Passerini, J. Hassoun, A new, high energy Sn–C/$Li[Li_{0.2}Ni_{0.4/3}Co_{0.4/3}Mn_{1.6/3}]O_2$ lithium-ion battery, ACS Appl. Mater. Interfaces 6 (2014) 12956–12961, https://doi.org/10.1021/am502884y.
[64] L. Fang, M. Chen, K.-.W. Nam, Y.-.M. Kang, Redox evolution of Li-rich layered cathode materials, Batteries 8 (2022) 132, https://doi.org/10.3390/batteries8100132.
[65] N. Yabuuchi, K. Yoshii, S.T. Myung, I. Nakai, S. Komaba, Detailed studies of a high-capacity electrode material for rechargeable batteries, Li_2MnO_3-$LiCo_{1/3}Ni_{1/3}Mn_{1/3}O_2$, J. Am. Chem. Soc. 133 (2011) 4404–4419, https://doi.org/10.1021/ja108588y.
[66] M.N. Ates, S. Mukerjee, K.M. Abraham, A Li-rich layered cathode material with enhanced structural stability and rate capability for Li-on batteries, J. Electrochem. Soc. 161 (2014) A355–A363, https://doi.org/10.1149/2.070403jes.
[67] S. Tan, Z. Zhang, Y. Li, Y. Li, J. Zheng, Z. Zhou, Y. Yang, Tris(hexafluoro-iso-propyl)phosphate as an SEI-forming additive on improving the electrochemical performance of the $Li[Li_{0.2}Mn_{0.56}Ni_{0.16}Co_{0.08}]O_2$ cathode material, J. Electrochem. Soc. 160 (2013) A285–A292, https://doi.org/10.1149/2.066302jes.
[68] J. Chen, H. Yang, T. Li, C. Liu, H. Tong, J. Chen, Z. Liu, L. Xia, Z. Chen, J. Duan, L. Li, The effects of reversibility of H2-H3 phase transition on Ni-rich layered oxide cathode for high-energy lithium-ion batteries, Front. Chem. 7 (2019) 1–10, https://doi.org/10.3389/fchem.2019.00500.
[69] T. Aida, T. Toma, S. Kanada, A comparative study of particle size and hollowness of $LiNi_{1/3}Co_{1/3}Mn_{1/3}O_2$ cathode materials for high-power Li-ion batteries: effects on electrochemical performance, J. Solid State Electrochem. 24 (2020) 1415–1425, https://doi.org/10.1007/s10008-020-04640-z.
[70] L. Zhu, C. Bao, L. Xie, X. Yang, X. Cao, Review of synthesis and structural optimization of $LiNi_{1/3}Co_{1/3}Mn_{1/3}O_2$ cathode materials for lithium-ion batteries applications, J. Alloys Compd. 831 (2020), 154864, https://doi.org/10.1016/j.jallcom.2020.154864.
[71] S. Liu, B. Wang, X. Zhang, S. Zhao, Z. Zhang, H. Yu, Reviving the lithium-manganese-based layered oxide cathodes for lithium-ion batteries, Matter 4 (2021) 1511–1527, https://doi.org/10.1016/j.matt.2021.02.023.
[72] H. Sun, K. Zhao, Electronic structure and comparative properties of $LiNi_xMn_yCo_zO_2$ cathode materials, J. Phys. Chem. C 121 (2017) 6002–6010, https://doi.org/10.1021/acs.jpcc.7b00810.
[73] D. Di Lecce, V. Marangon, M. Isaacs, R. Palgrave, P.R. Shearing, J. Hassoun, Degradation of layered oxide cathode in a sodium battery: a detailed investigation by X-ray tomography at the nanoscale, Small Methods 5 (2021), 2100596, https://doi.org/10.1002/smtd.202100596.
[74] Y.-.F. Deng, S.-.X. Zhao, Y.-.H. Xu, C.-.W. Nan, Electrochemical performance of layer–spinel composite cathode materials at elevated temperature and high rate, Appl. Surf. Sci. 351 (2015) 209–215, https://doi.org/10.1016/j.apsusc.2015.05.132.
[75] B. Scrosati, J. Garche, Lithium batteries: status, prospects and future, J. Power Sources 195 (2010) 2419–2430, https://doi.org/10.1016/j.jpowsour.2009.11.048.
[76] J.B. Goodenough, K.-.S. Park, The Li-ion rechargeable battery: a perspective, J. Am. Chem. Soc. 135 (2013) 1167–1176, https://doi.org/10.1021/ja3091438.
[77] J. Hassoun, K.S. Lee, Y.K. Sun, B. Scrosati, An advanced lithium ion battery based on high performance electrode materials, J. Am. Chem. Soc. 133 (2011) 3139–3143, https://doi.org/10.1021/ja110522x.
[78] G. Gabrielli, M. Marinaro, M. Mancini, P. Axmann, M. Wohlfahrt-Mehrens, A new approach for compensating the irreversible capacity loss of high-energy Si/C|$LiNi_{0.5}Mn_{1.5}O_4$ lithium-ion batteries, J. Power Sources 351 (2017) 35–44, https://doi.org/10.1016/j.jpowsour.2017.03.051.
[79] D. Aurbach, Review of selected electrode–solution interactions which determine the performance of Li and Li ion batteries, J. Power Sources 89 (2000) 206–218, https://doi.org/10.1016/S0378-7753(00)00431-6.
[80] K. Xu, Electrolytes and interphases in Li-ion batteries and beyond, Chem. Rev. 114 (2014) 11503–11618, https://doi.org/10.1021/cr500003w.